Electronic Supplementary Material (ESI) for Journal of Materials Chemistry A.

Supplementary information

Boosting Oxygen Evolution Reaction Performance via Metal Defect-Induced Lattice Oxygen Redox Reactions on Spinel Oxides

Jingxuan Zheng [a], Rui Sun[b], DaPeng Meng [a], Junxin Guo [a] and Zhao Wang [a],*

[a] *National Engineering Research Center of Industry Crystallization Technology, School of Chemical Engineering and Technology, Tianjin University, Tianjin 300072, China.*

[b] *Tianjin Academy of Eco-Environmental Sciences, Tianjin, 300191, China*

Corresponding authors
Prof. Zhao Wang, Email: **wangzhao@tju.edu.cn**

This Supporting Information file includes:

Experimental detail

Chemicals and reagents

$Zn(NO_3)_2·6H_2O$, $Fe(NO_3)_2·9H_2O$, NH_4F and urea were all analytical grade purity from Aladdin Reagent (Shanghai) Co., Ltd. The Ni foam was purchased from Changde Liyuan New Materials Co., Ltd. Reagents were used as received without further purification.

Synthesis of $ZnFe_2O_4$

In a typical method to synthesize $ZnFe_2O_4$ spinel nanosheet, 0.297 g $Zn(NO_3)_2·6H_2O$, 0.808 g $Fe(NO_3)_2·9H_2O$, 0.296 g NH_4F and 2.88 g urea were dissolved into 160 mL of deionized water under vigorous agitation. Subsequently, the solution was transferred to a 200 mL Teflon-lined stainless-steel autoclave and pre-treated nickel foam (1 cm*1 cm*1.5 mm, 97.2 % porosity) was immersed in solution, which was kept at 140 °C for 4 h. After it was cooled to room temperature, the Ni foam was washed with deionized water and ethanol, and dried at 60 °C overnight. The sample was heated in air at 400 ℃ for 2 h with a heating rate of 5 °C min^{-1} to produce $ZnFe_2O_4$ nanosheets, which was name as ZnFeO-C.

To prepare the samples, an excess amount of NaOH was placed into a mortar and thoroughly ground to a powder. Then, ZnFeO-C was combined with a significant quantity of powdered NaOH, and the NaOH powder was attached to the surface of ZnFeO-C by shaking. Subsequently, the ZnFeO-C with the adhered NaOH powder was transferred to a dielectric barrier discharge plasma reactor. The mixture was then treated in an oxygen atmosphere at 100 V and 2 A for 15 and 30 minutes, resulting in samples named ZnFeO-CP-15 and ZnFeO-CP-30, respectively. In addition, samples with decreased Zn content (0.148 g $Zn(NO_3)_2\cdot6H_2O$) were also prepared and denoted as ZnFeO-0.25-C and ZnFeO-0.25-CP -15.

Characterization

The crystalline structure analysis were characterized by power X-ray diffraction (XRD) on Rigaku D/M 2500 using a Cu Kα1 source with a scanning rate of 8 $°\cdot min^{-1}$. Scanning electron microscope (SEM) and High-resolution transmission electron microscopy (TEM) analysis was carried out using a hitachi SU8100 and Tecnai G2 F20. X-ray photoelectron spectroscopy (XPS) and ultraviolet photoelectron spectroscopy (UPS) were performed by a Thermo-Fisher ESCALAB-250Xi with a monochromatic Al Kα source (1486.6 eV) and He I (21.22 eV), respectively. The adventitious carbon C1s used for XPS element correction is located at 284.8 eV. The UPS spectra were calibrated by the work function of Au (5.1 eV). X-ray absorption near-edge spectra and extended X- Ray absorption fine structure (XANES and EXAFS, Fe K-edge) were performed in transmission mode for the bulk at the Super Photon ring-8 GeV in Harima Science Garden City, Hyogo. The storage ring runs 8 GeV electrons at 99.6 mA constantly during the experiments. The incident beam was monochromated by Si (111) double-crystal monochromators. The XANES and EXAFS data obtained in the experiment were analyzed and fitted with the Athena and Artemis code packages in Demeter [1]. To determine the catalyst loadings and metal content in the electrolyte, Inductively Coupled Plasma Optical Emission Spectrometer (ICPOES) tests were conducted using the Agilent ICPOES 730 instrument. For the ICP characterization, a 1 mL sample was collected at each designated time point (0 s, 1200 s, 2400 s, 3600 s, 7200 s, 14400 s, 25200 s). During the ICP characterization process, 0.5 mL of the electrolyte was directly taken and introduced into the instrument for testing. The instrument provides the direct measurement of the element's concentration in mg/L in the electrolyte.

Electrochemical measurements

The cyclic voltammetry curves (CV), linear sweep voltammograms (LSVs) and electrochemical impedance spectroscopy (EIS, 5 mV amplitude 0.1−100k Hz frequency) tests were performed in a conventional three-electrode system in 1 mol/L KOH with Princeton Applied Research VersaSTAT 3. The electrochemical cell was assembled with the obtained catalyst (The loadings of ZnFeO-C, ZnFeO-CP-15 and ZnFeO-CP-30 were 0.874, 0.710 and 0.522 mg/cm^2, respectively), Hg|HgO (in 1 mol/L KOH) and a graphite rod as work electrode, reference electrode and counter electrode, respectively. To prepare the RuO_2 electrode, the catalyst (20 mg) was ultrasonically dispersed in a solution containing 3000 μL of ultrapure water (18.2 MΩ·cm), 1000 μL isopropanol and 200 μL of 5% Nafion (Sigma Aldrich, USA). The nickel foam substrate was treated by carefully immersing it, approximately 1 cm deep, into the ink solution using tweezers. The coated foam was then dried, and this process was repeated ten times to achieve a working nickel foam electrode loaded with commercial RuO2 at a loading of 0.73 mg cm^{-2}. All the LSV plots were collected at 5 mV·s^{-1} and then were corrected for the iR compensation. The measured potentials vs. Hg/HgO were converted to a reversible hydrogen electrode (RHE) scale according to the Nernst equation (E_{RHE}

$=E_{Hg/HgO} + 0.098+0.0592 \times pH$). The electrochemical active surface area (ECSA) was evaluated by the electrochemical double-layered capacitance (C_{dl}) by measuring the capacitive current associated with double-layer charging from the scan-rate dependence of CVs (10, 20, 50, 100 and 200 mV/s) [2]. This non-redox region was selected to a 0.1 V window in the range of 0.927-1.027 V *vs*. RHE. The Cdl can be gained from the linear slope by plotting the different in current density within selected potential against the scan rates. ECSA for all prepared catalysts was calculated by follow equation:

$$\mathrm{ECSA} = \frac{\mathrm{C_{dl,cat}\ (mF/cm^2)}}{\mathrm{C_{dl,std}\ (mF/cm^2)}}$$

Where the $C_{dl,\ std}$ corresponds to the specific capacitance of an atomically smooth material and is approximately equal to 60 μF/cm^2 according to previous reports.

DFT calculation

All the calculations were carried out by a plane-wave technique with GGA-PBE to describe the exchange and correlation terms in the Vienna Ab initio Simulation Package (VASP) [3-5]. The projector augmented wave (PAW) pseudo-potential was used to describe the core electrons [6, 7]. All calculations were performed using a cutoff energy of 520 eV with smearing of 0.05 eV. In order to correctly describe the electronic structure of the Fe-3d state, the GGA + U method was used. The U-J value of Fe was selected as 5.3 eV [8]. The vdW corrections were calculated with zero damping DFT-D3 method of Grimme [9, 10]. A G-centered 3 × 3 × 3 and 3 × 4× 1 k mesh was used in cell and slabs calculations, respectively. The accurate precision of convergence for the geometry optimization were set to 10^{-5} eV for energy change, all atomic structures were fully optimized until the Hellmann−Feynman forces were smaller than 0.05 eV/Å.

Spin polarization and dipole corrections were considered in all calculations. All periodic slabs included 7 layers of atoms and a 15 Å thick vacuum layer, and constrainted the bottom layer atoms and relax the top 5 layers of atoms on the surface. In addition, the tetrahedral method and an additional support grid was used in single-point energies calculation.

The (110) plane was chosen as the active surface to study the electronic structure of the catalyst and the electrochemical reaction process because it is considered to be be a crucial role in the spinel [11]. The geometric structure models of ZnFeO-C, ZnFeO-CP-15 and ZnFeO-CP-30 (110) planes were shown in Figure S1. The typical absorbate evolution mechanism (AEM) calculation used the thermodynamic model proposed by Nøskov et al [12]. The lattice oxygen-mediated mechanism (LOM) model referred to the work of Zhu et al [13]. Models of all intermediates of AEM and LOM were shown in Figure S2 and S3. The adsorption energy of intermediate on the catalyst surface could be calculated by the following equations:

$$\Delta E_{\mathrm{ads}^*} = E\,(\mathrm{ads}^*) - E\,(^*) - E\,(\mathrm{ads})$$

Where the * represented the active site of the catalyst surface, ads represented the intermediate, and ads* represented the intermediate adsorbed on the active site of the catalyst

The free energy of intermediate adsorption was calculated by the following equations:

$$\Delta G_{\mathrm{ads}} = \Delta E_{\mathrm{ads}} + \Delta E_{\mathrm{ZPE}} + \Delta U_{(0\rightarrow \mathrm{T})} - \mathrm{T}\Delta S \text{ [14]}$$

Where ΔG_{ads} represented the free energy of intermediate. The $\Delta E_{\mathrm{ZPE}} + \Delta U_{(0\rightarrow \mathrm{T})} - \mathrm{T}\Delta S$ was obtained by VASPKIT processing the result of frequency calculation (Table S7)

[14].

Then the theoretical overpotentials for OER could be calculated using the equations:

$$\eta = \Delta G_{\mathrm{max}}/e - 1.23 \quad (\mathrm{V})$$

In accordance with the computational hydrogen electrode (CHE) model, the chemical potential of H^+ and e^- was related to that of $1/2H_2$ (g) [12, 15]. Meanwhile, the effects of electrode potential (U) could be treated as an energy shift to free energy change.

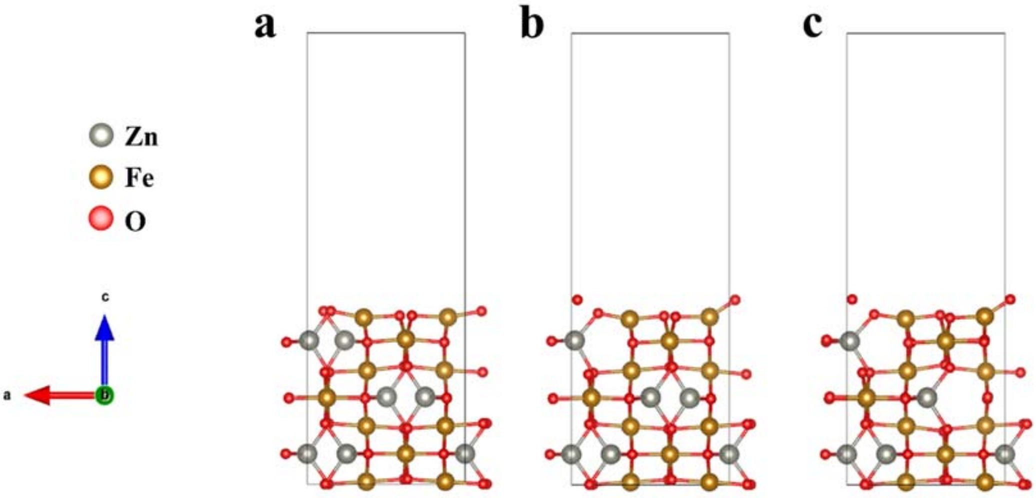

Figure S1 Side views for the of (110) slabs of (a) ZnFeO-C, (b) ZnFeO-CP-15 and (c) ZnFeO-CP-30, respectively.

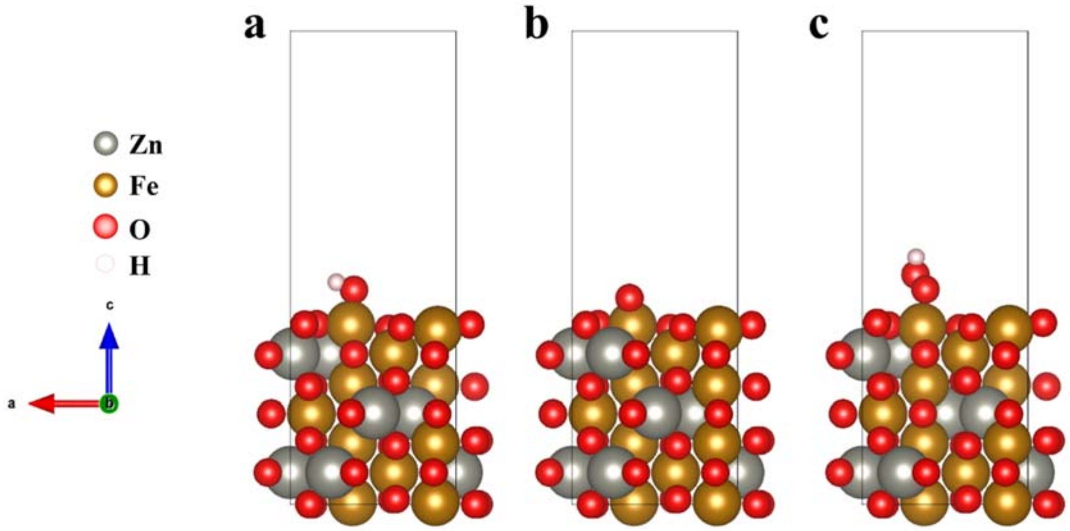

Figure S2 The structural optimizational model of AEM.

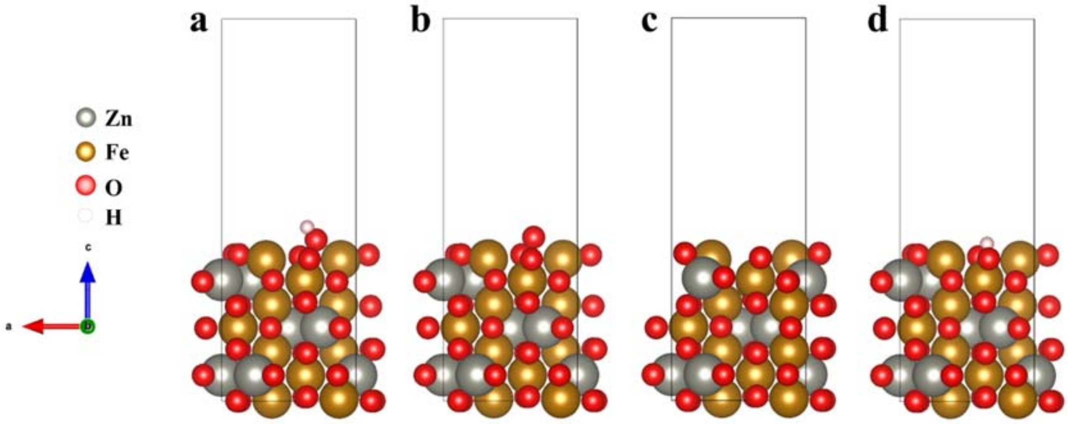

Figure S3 The structural optimizational model of LOM.

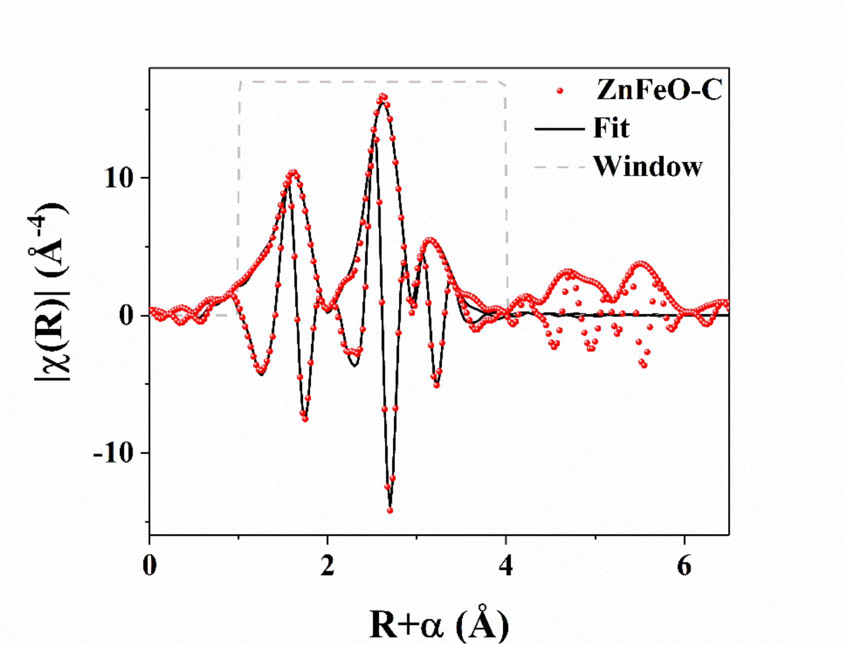

Figure S4. Fitted curves of EXAFS curve in R-space of ZnFeO-C.

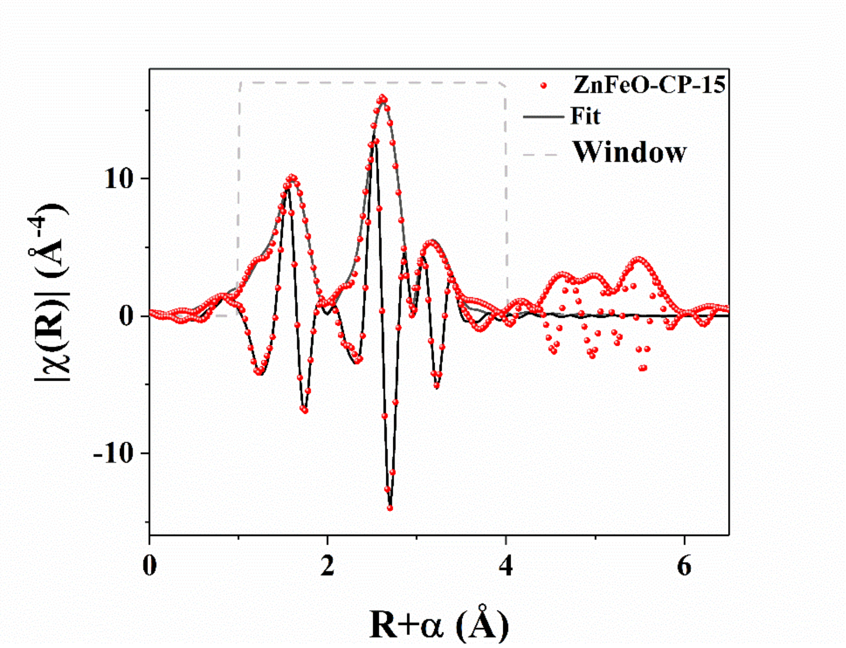

Figure S5. Fitted curves of EXAFS curve in R-space of ZnFeO-CP-15.

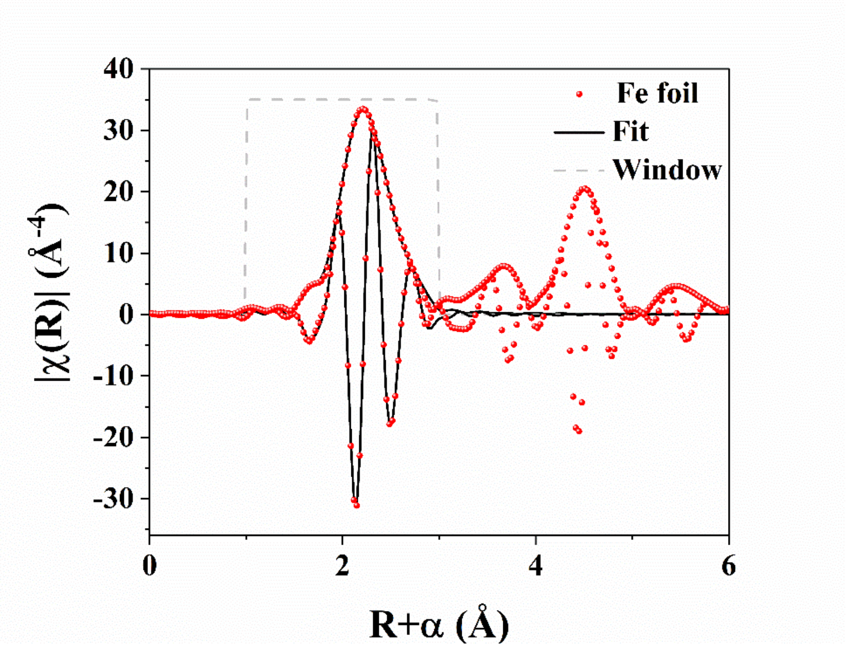

Figure S6. Fitted curves of EXAFS curve in R-space of Fe foil.

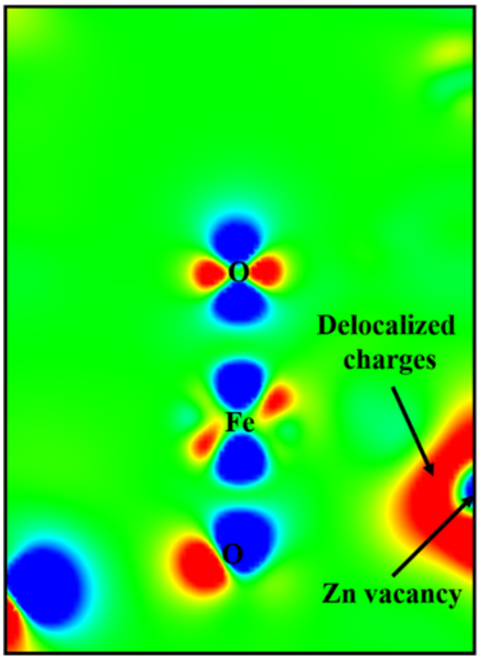

Figure S7. Two-dimensional section of charge density difference distribution (between catalyst with and without one metal vacancy on the (110) surface) for $ZnFe_2O_4$.

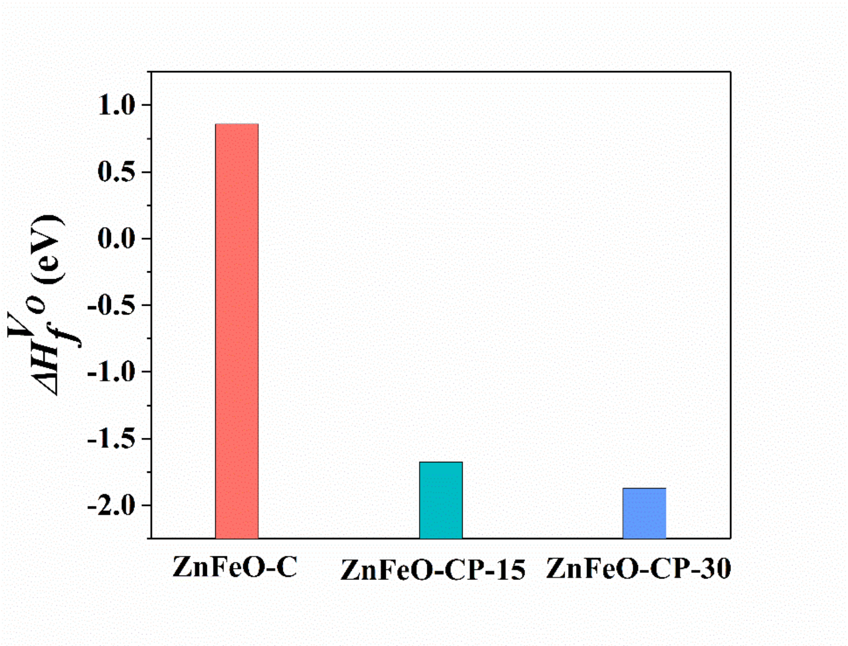

Figure S8. The modeling results of ZnFeO-C, ZnFeO-CP-15 and ZnFeO-CP-30 for oxygen defect formation enthalpy ($\Delta H_f^{V_O}$).

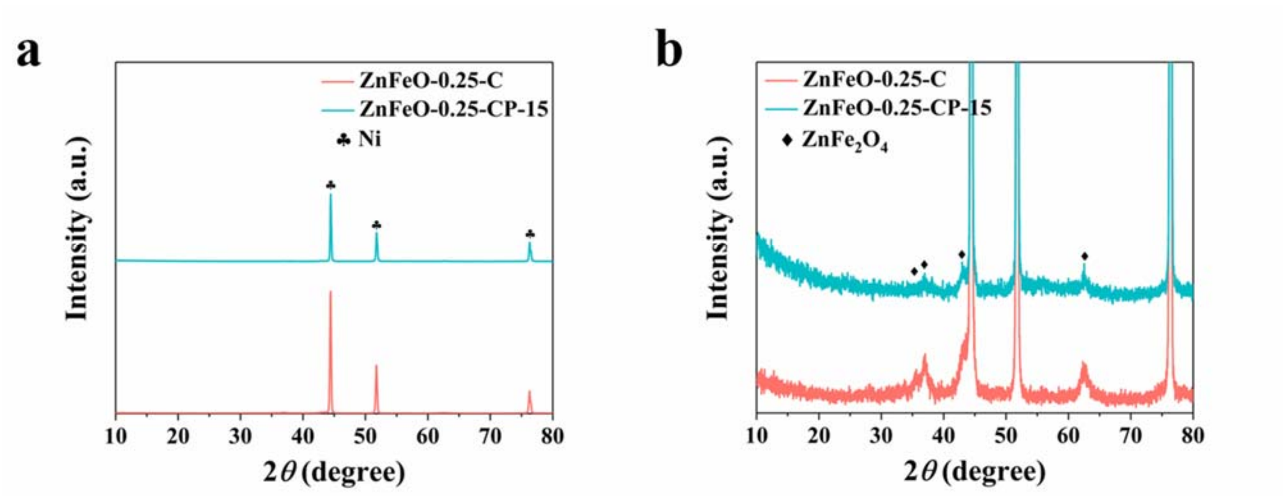

Figure S9. (a) XRD patterns of ZnFeO-0.25-C and ZnFeO-0.25-CP-15. (b) Larger scale of XRD patterns.

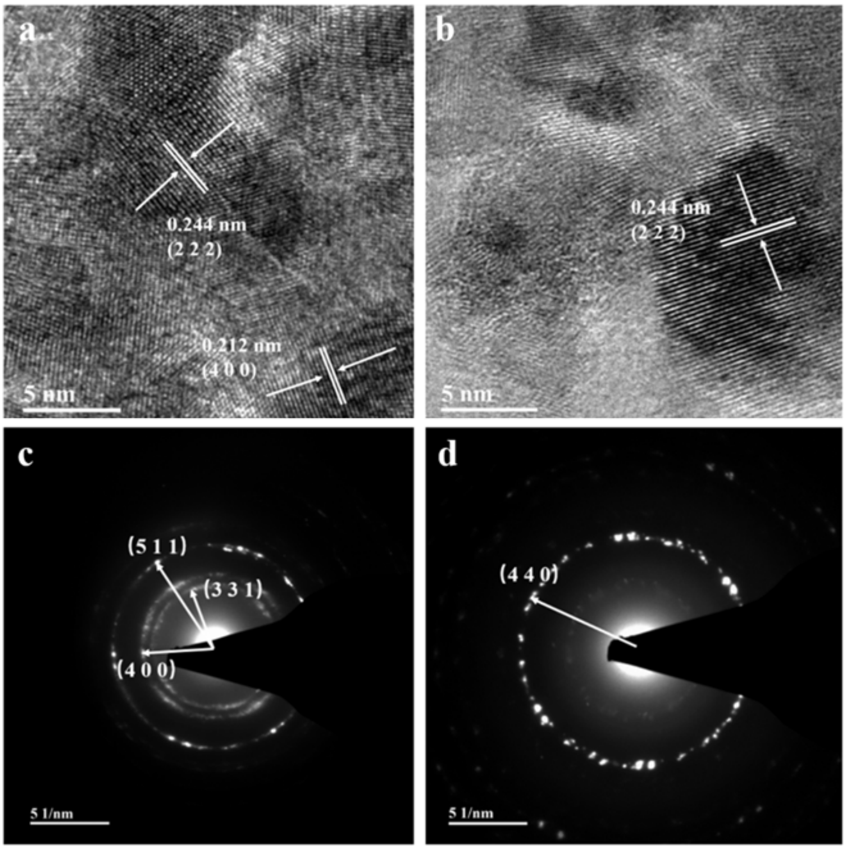

Figure S10. TEM images of (a) ZnFeO-0.25-C and (b) ZnFeO-0.25-CP-15. Selected area electron diffraction (SAED) images of (c) ZnFeO-0.25-C and (d) ZnFeO-0.25-CP-15.

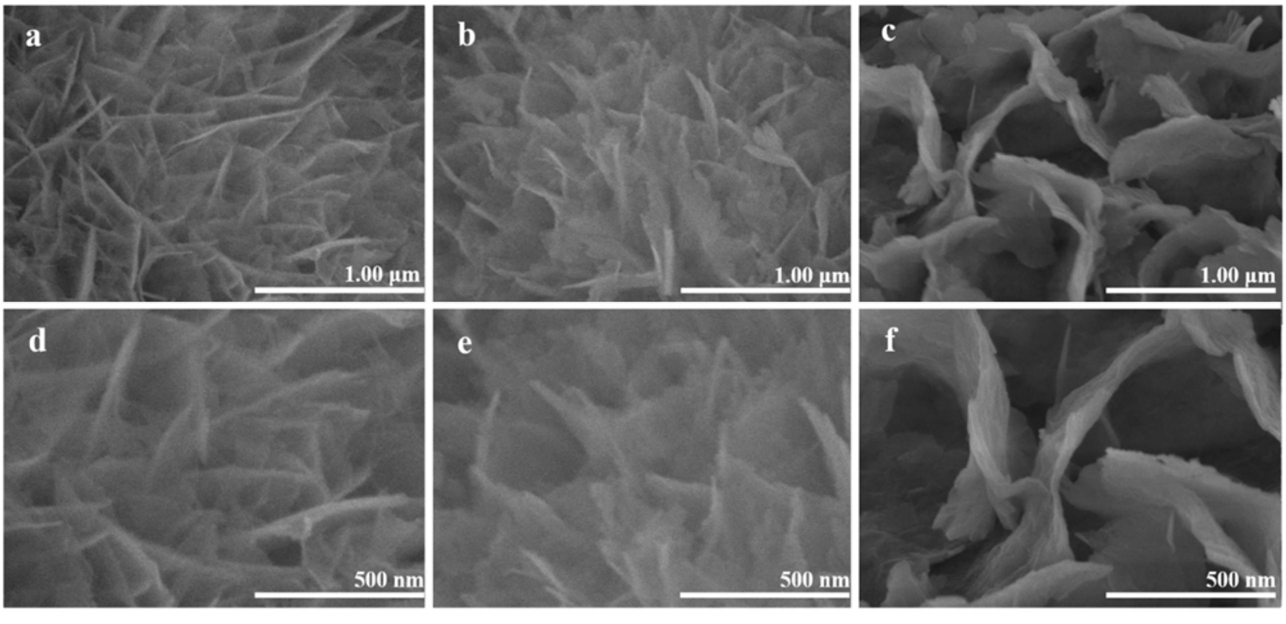

Figure S11. SEM images of (a), (d)ZnFeO-C, (b), (e) ZnFeO-CP-15 and (c), (f) ZnFeO-CP-30.

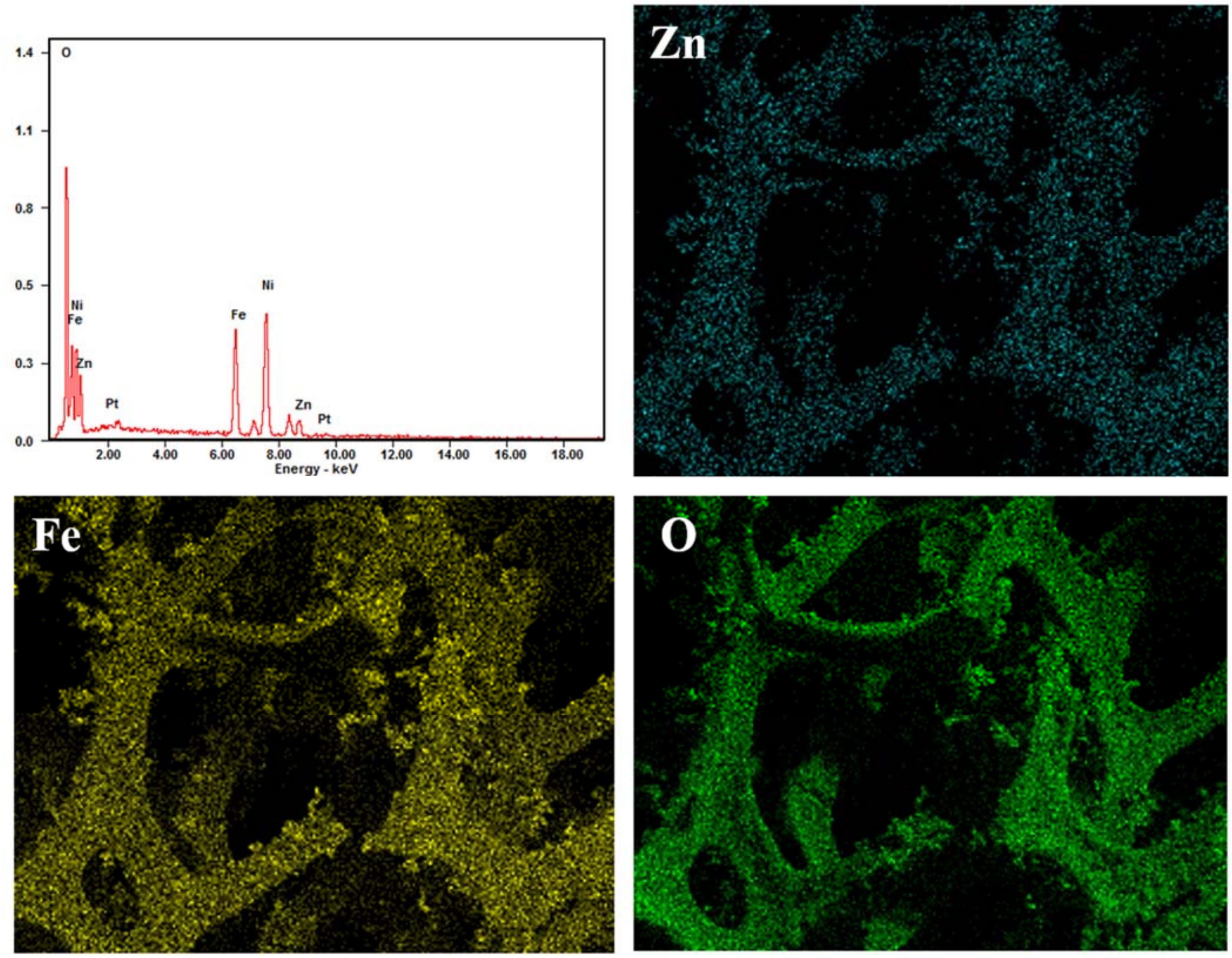

Figure S12. SEM-EDX mapping of Zn, Fe and O for ZnFeO-C.

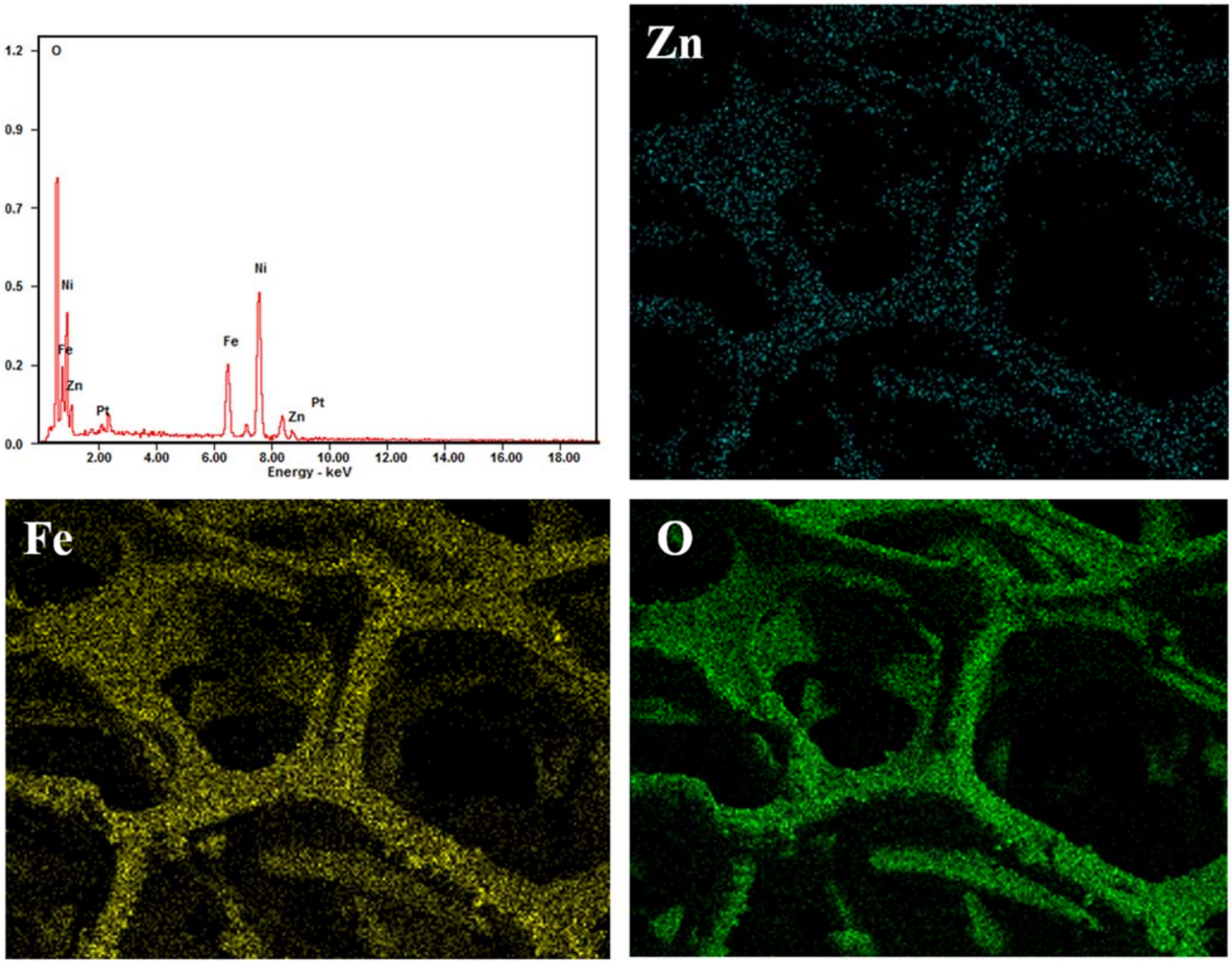

Figure S13. SEM-EDX mapping of Zn, Fe and O for ZnFeO-CP-15.

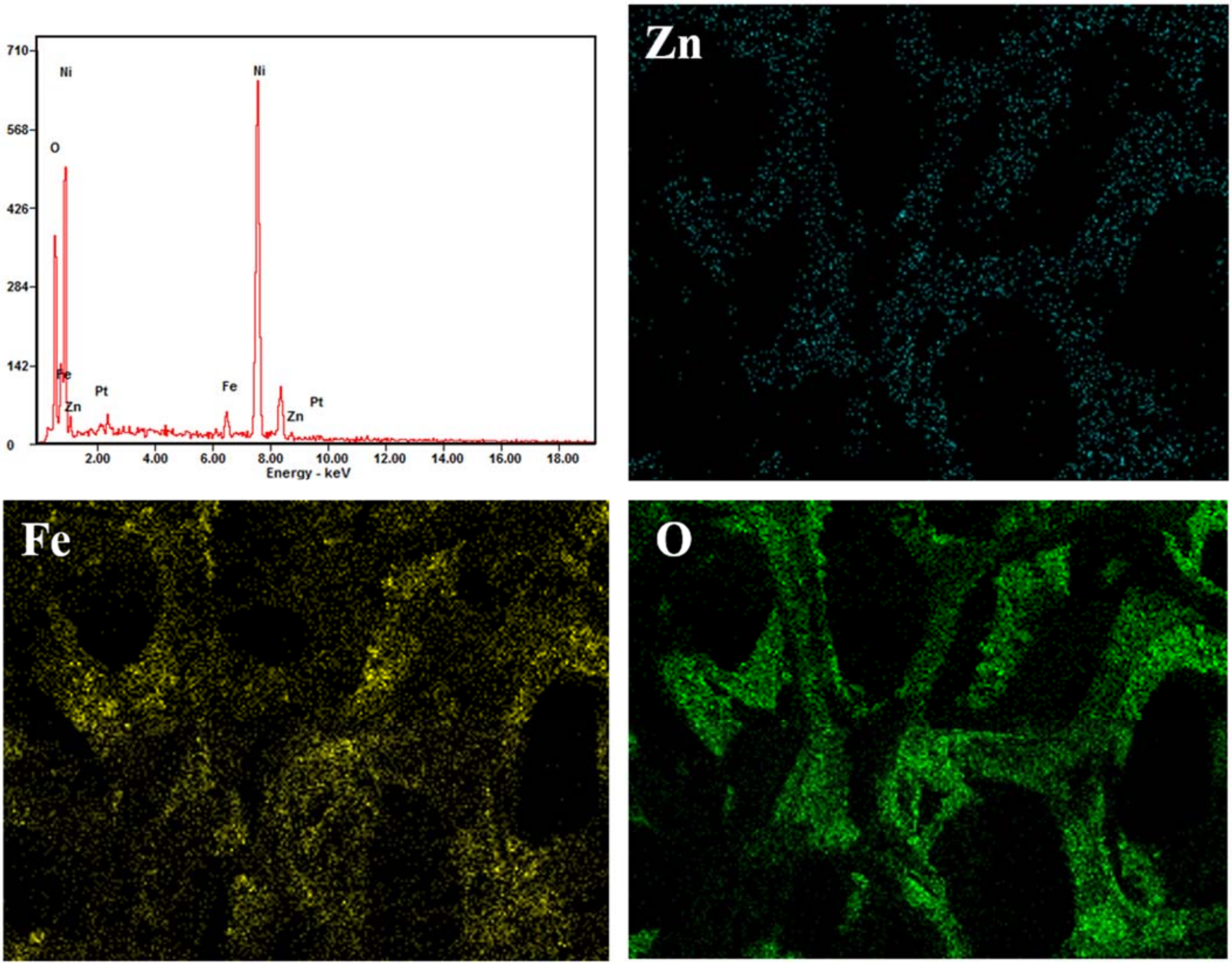

Figure S14. SEM-EDX mapping of Zn, Fe and O for ZnFeO-CP-30.

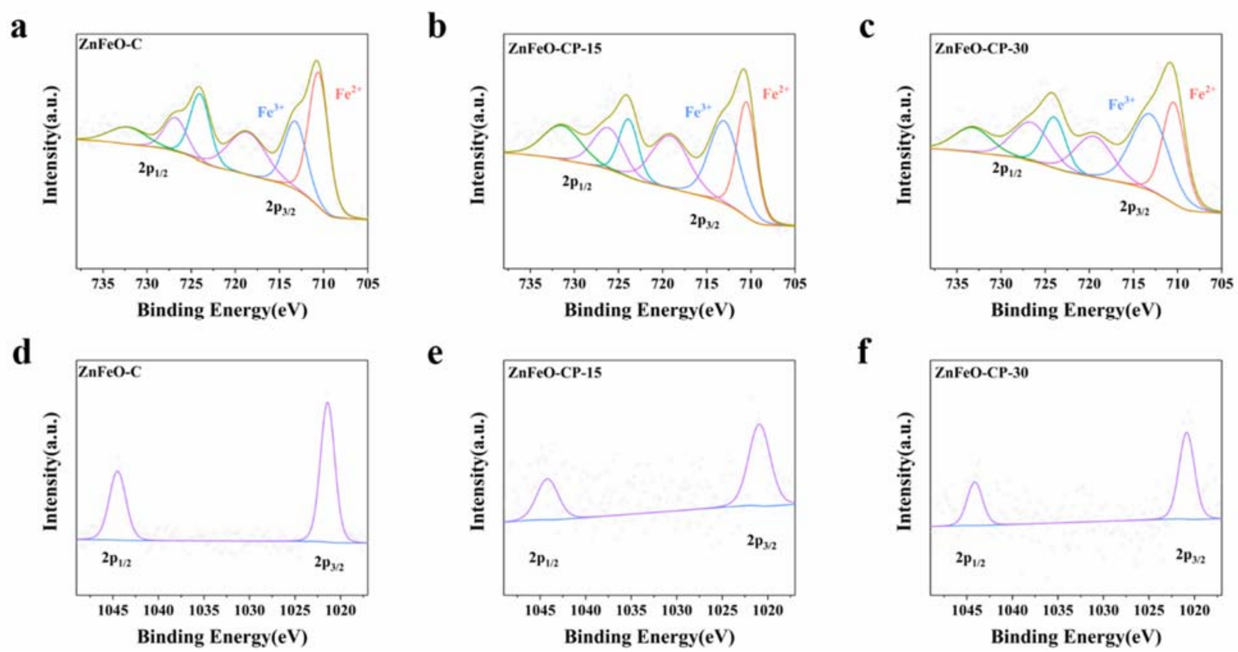

Figure S15. Deconvoluted Fe 2p spectra of (a) ZnFeO-C, (b) ZnFeO-CP-15 and (c) ZnFeO-CP-30.

Zn 2p spectra of (d) ZnFeO-C, (e) ZnFeO-CP-15 and (f) ZnFeO-CP-30.

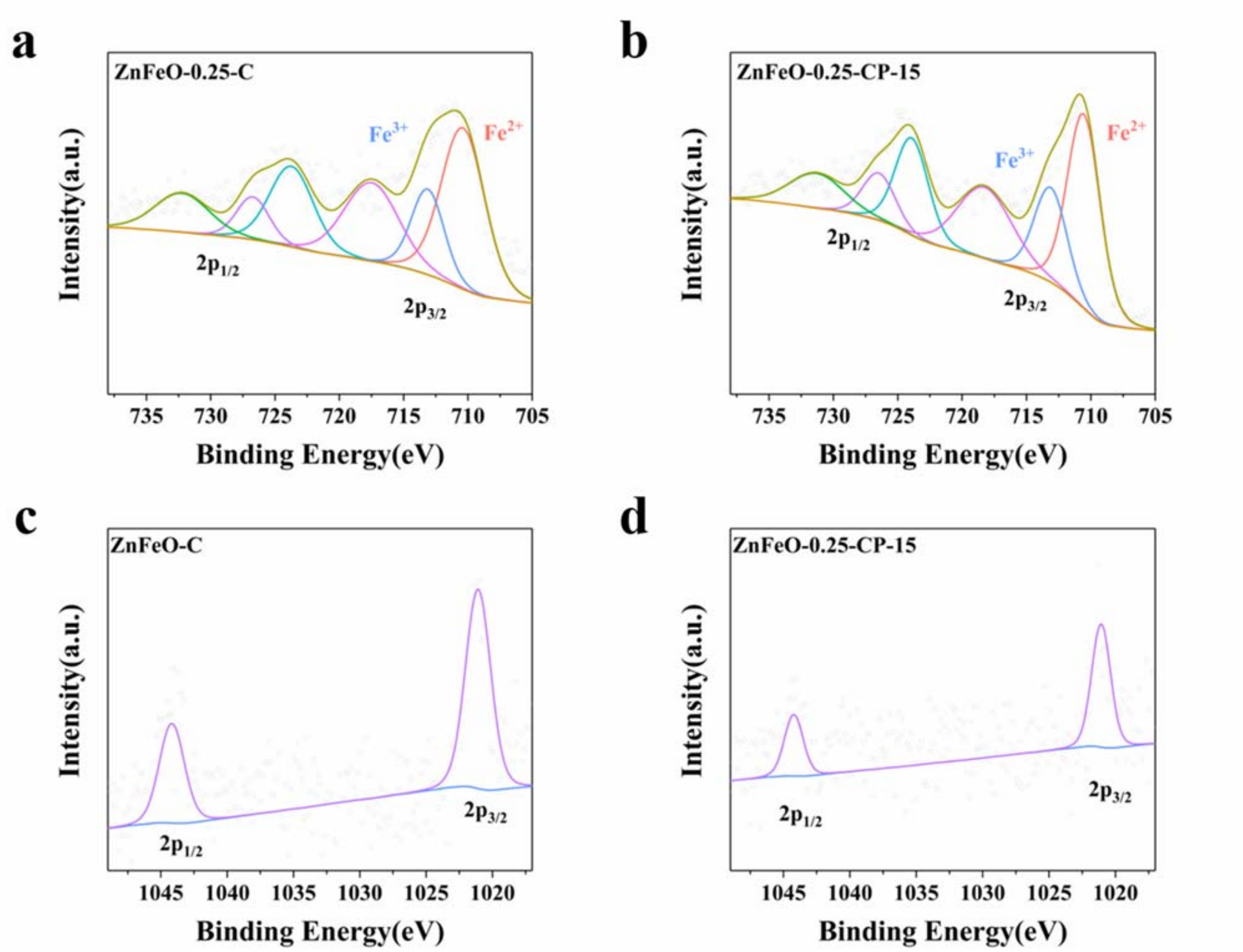

Figure S16. Deconvoluted Fe 2p spectra of (a) ZnFeO-0.25-C and (b) ZnFeO-0.25-CP-15. Zn 2p spectra of (c) ZnFeO-0.25-C and (d) ZnFeO-0.25-CP-15.

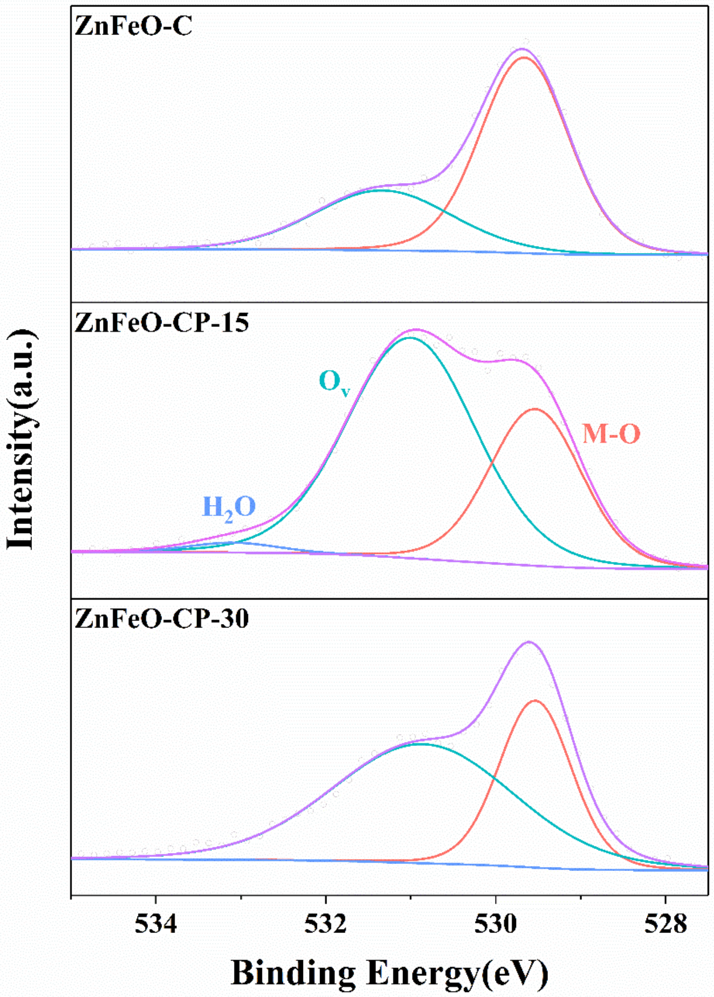

Figure S17. Deconvoluted O 1s spectra of ZnFeO-C, ZnFeO-CP-15 and ZnFeO-CP-30.

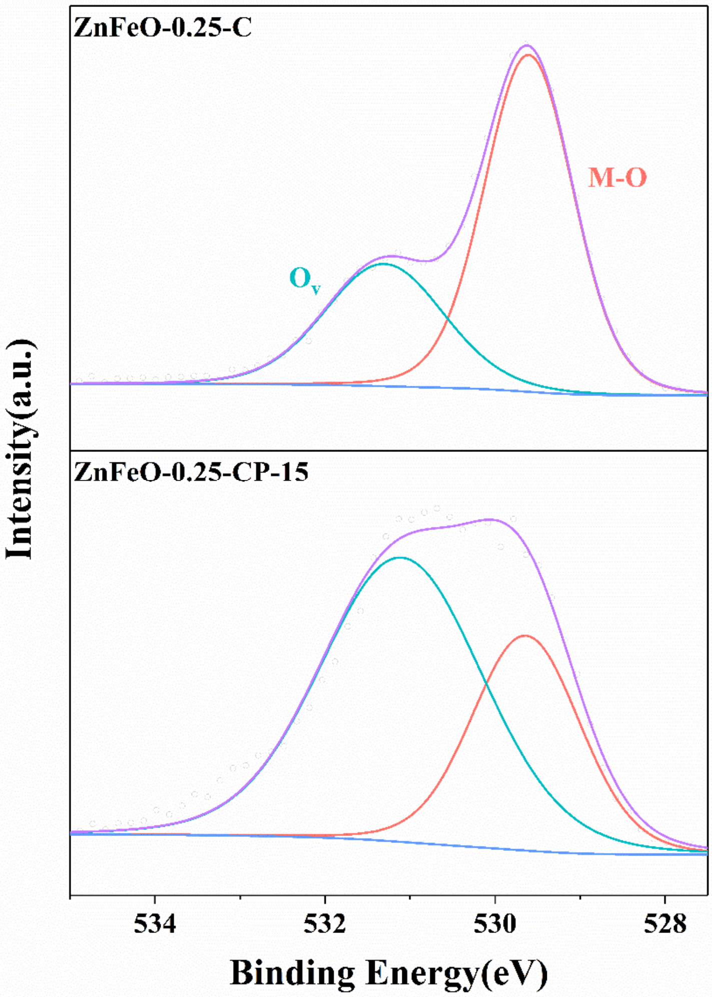

Figure S18. Deconvoluted O 1s spectra of ZnFeO-0.25-C and ZnFeO-0.25-CP-15.

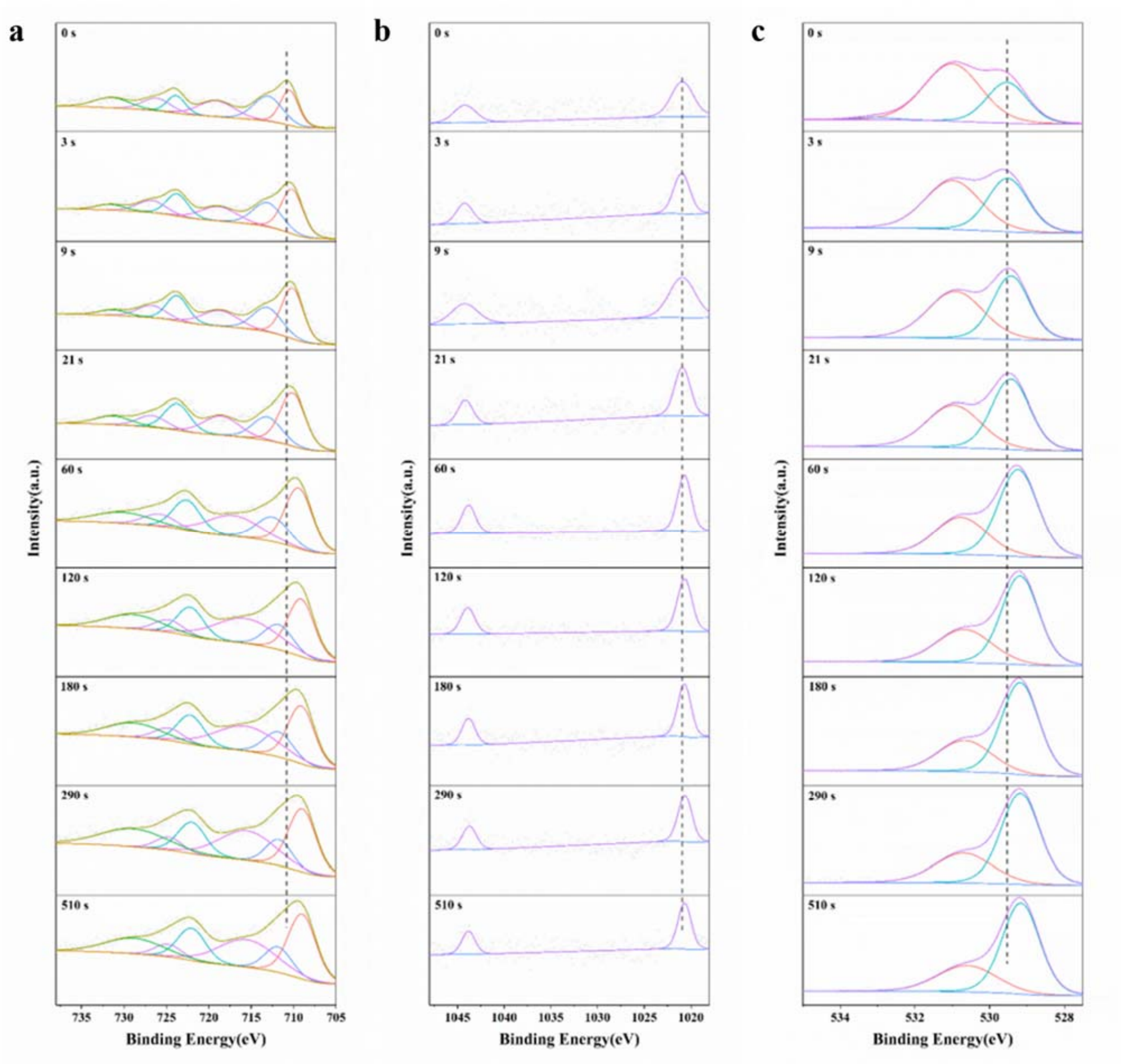

Figure S19. XPS depth profile of ZnFeO-CP-15: (a) Deconvoluted Fe 2p spectra. (b) Zn 2p spectra. (c) Deconvoluted O 1s spectra.

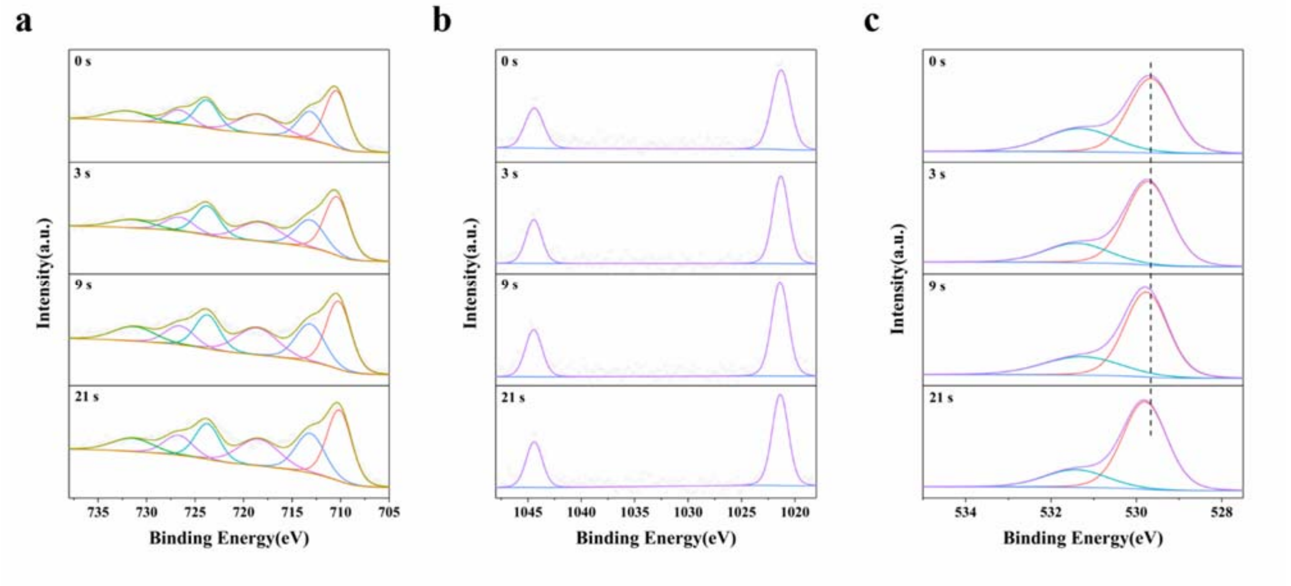

Figure S20. XPS depth profile of ZnFeO-C: (a) Deconvoluted Fe 2p spectra. (b) Zn 2p spectra. (c) Deconvoluted O 1s spectra.

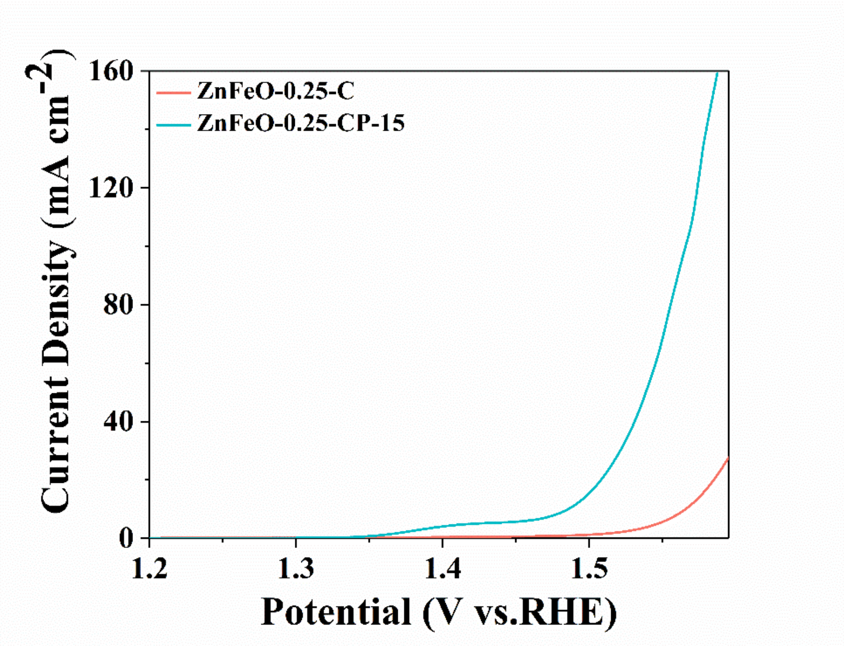

Figure S21. Polarization curves of OER on ZnFeO-0.25-C and ZnFeO-0.25-CP-15 in 1 M KOH (forward scan).

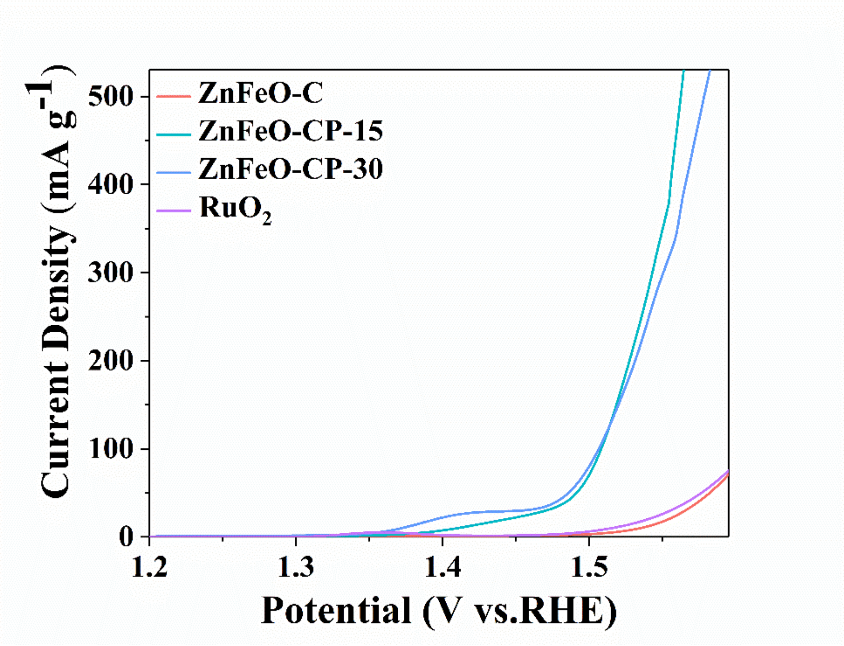

Figure S22. The mass activity ZnFeO-C, ZnFeO-CP-15, ZnFeO-CP-30 and RuO_2 in 1 M KOH recorded at 5 mV s^{-1} (forward scan).

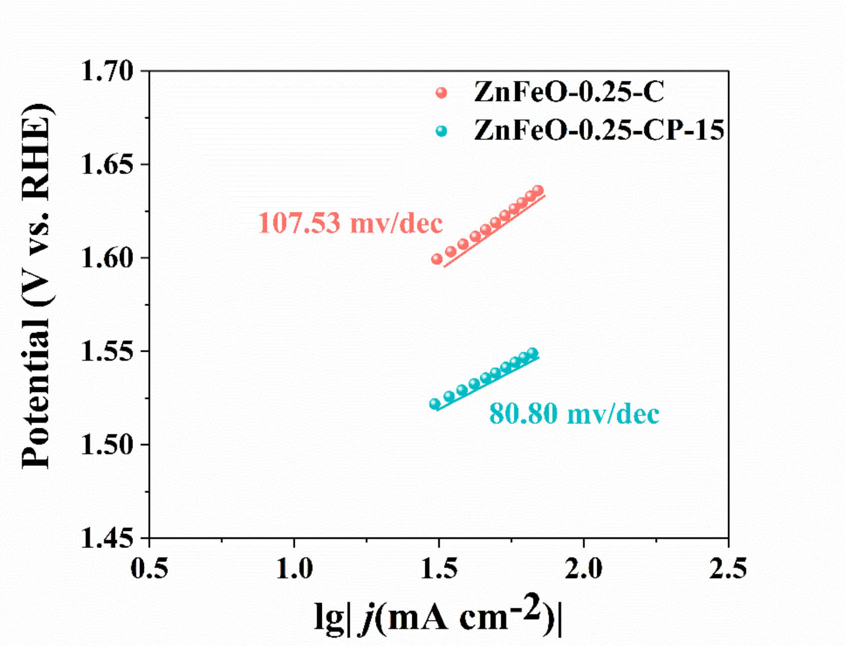

Figure S23. Tafel plots of ZnFeO-0.25-C and ZnFeO-0.25-CP-15.

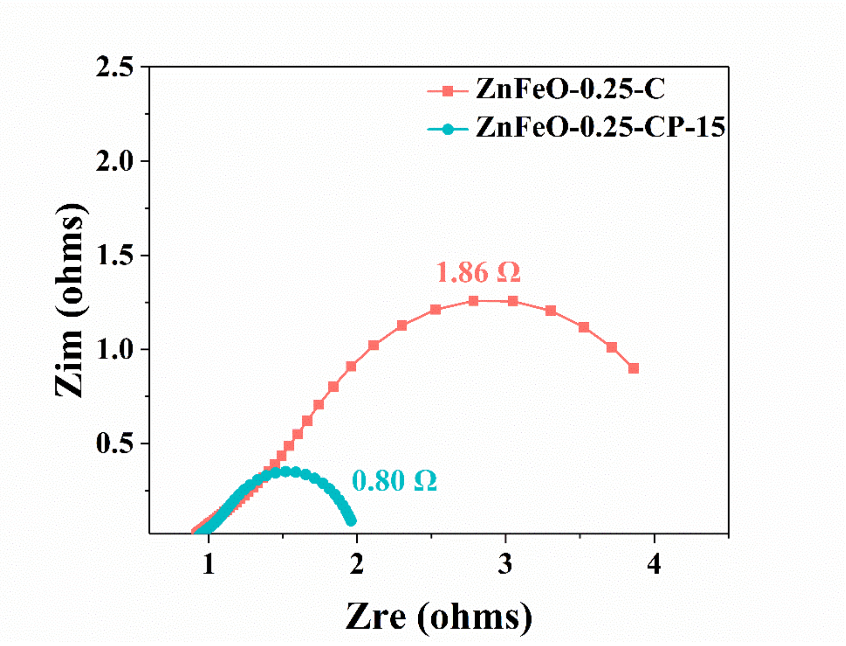

Figure S24. Electrochemical impedance spectroscopy of ZnFeO-0.25-C and ZnFeO-0.25-CP-15 at 1.46 V vs. RHE

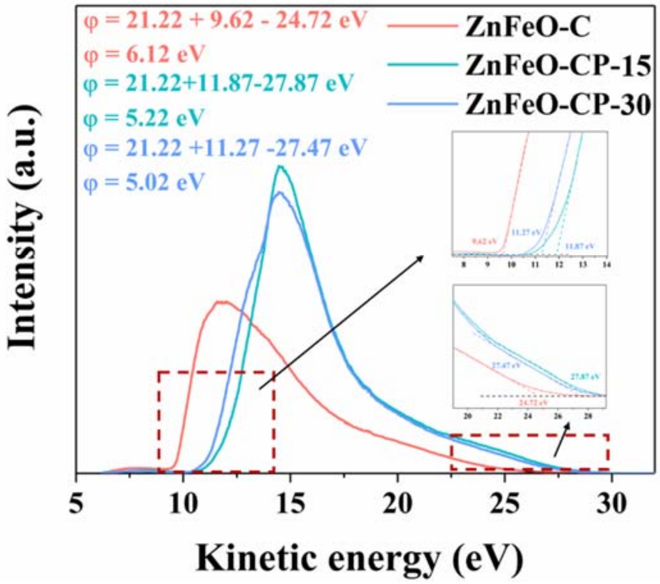

Figure S25. UPS spectra of ZnFeO-C, ZnFeO-CP-15 and ZnFeO-CP-30.

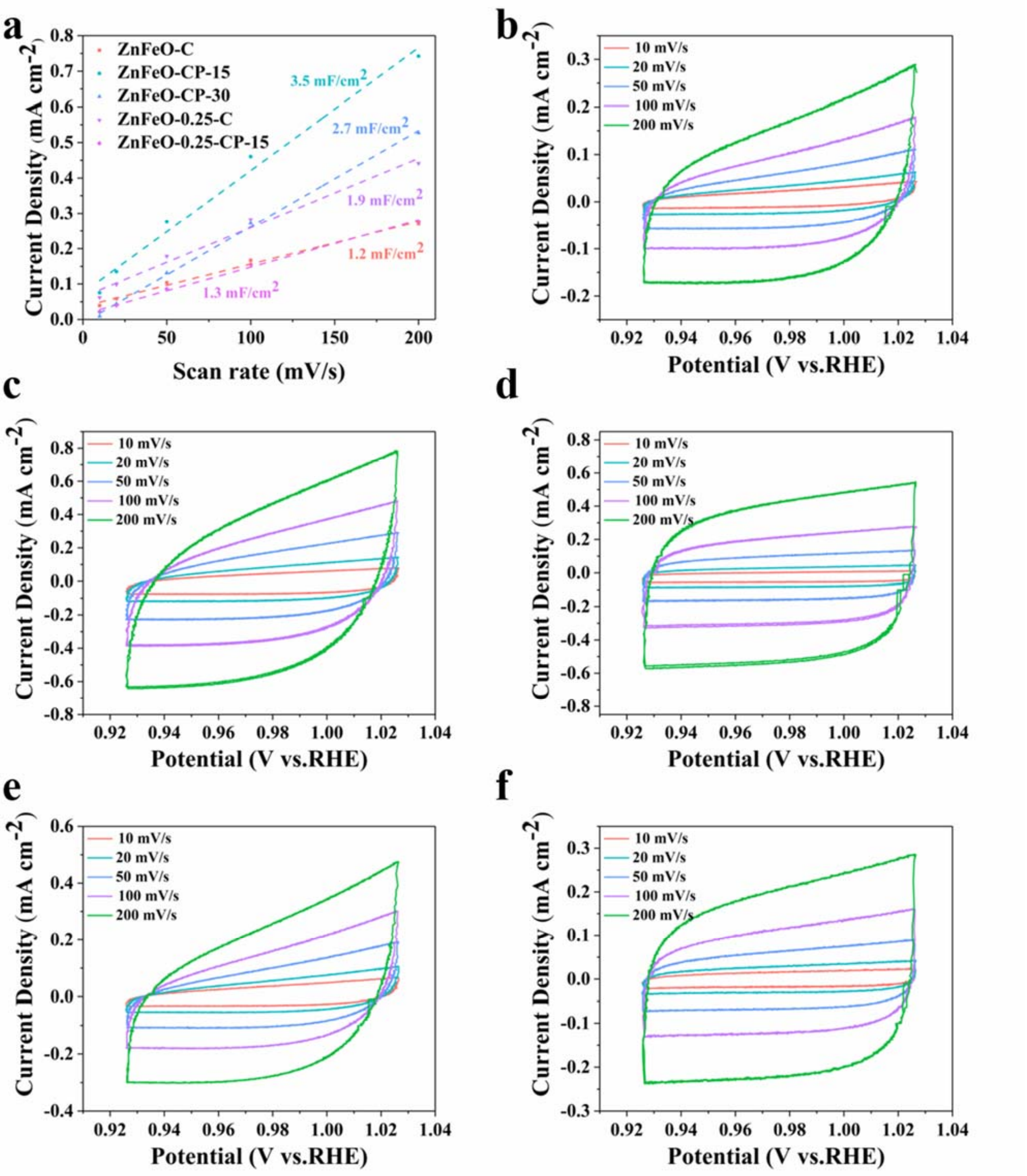

Figure S26. C_{dl} tests of all samples at 1.02 V. (a) C_{dl} determined by the capacitive currents. Cyclic voltammogram curves of (b) ZnFeO-C, (c) ZnFeO-CP-15, (d) ZnFeO-CP-30, (e) ZnFeO-0.25-C and (f) ZnFeO-0.25-CP-15 at multiple scan rates (10, 20, 50, 100 and 200 mV s^{-1}).

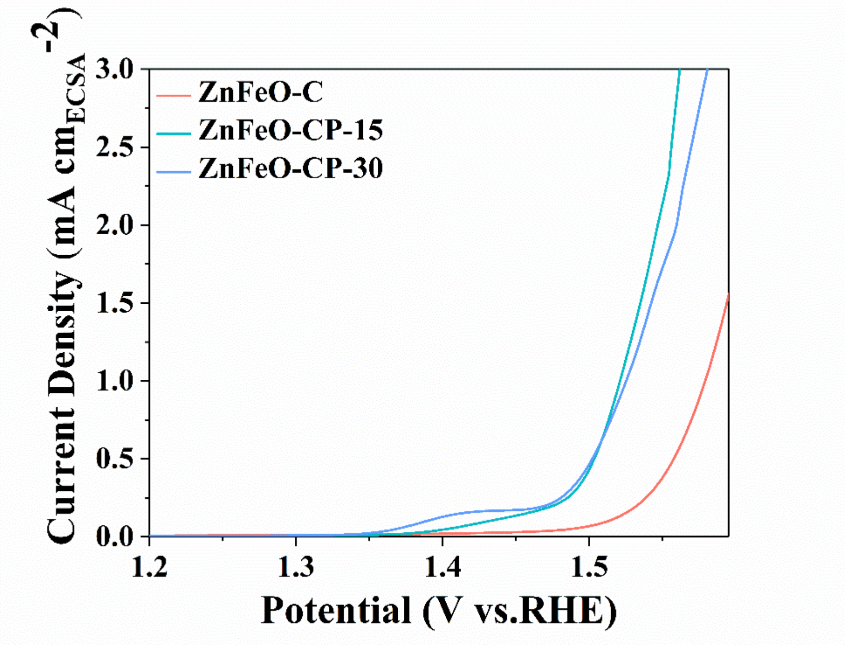

Figure S27. OER performance of ZnFeO-C, ZnFeO-CP-15 and ZnFeO-CP-30 after the electrochemical active area (ECSA) normalization

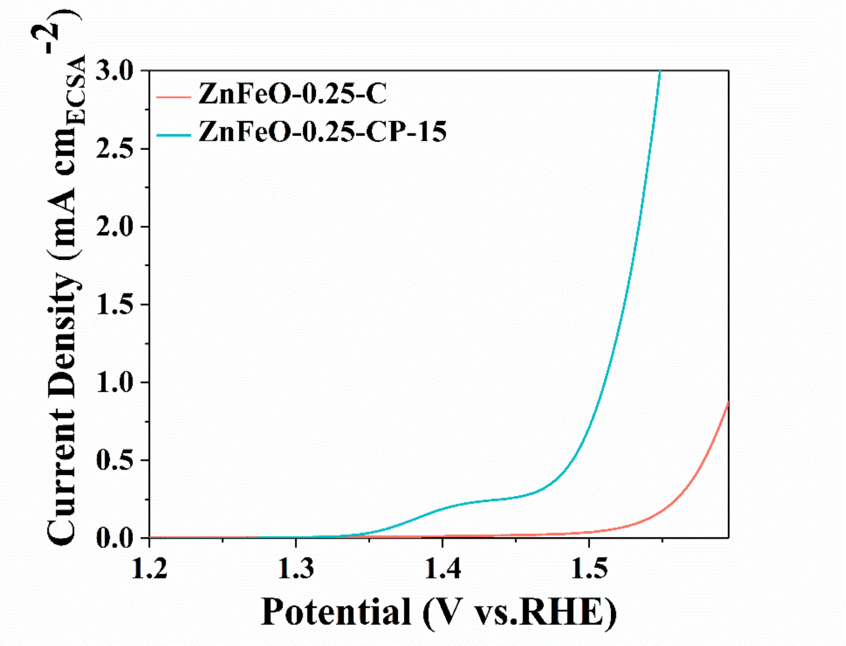

Figure S28. OER performance of ZnFeO-C, ZnFeO-CP-15 and ZnFeO-CP-30 after the electrochemical active area (ECSA) normalization

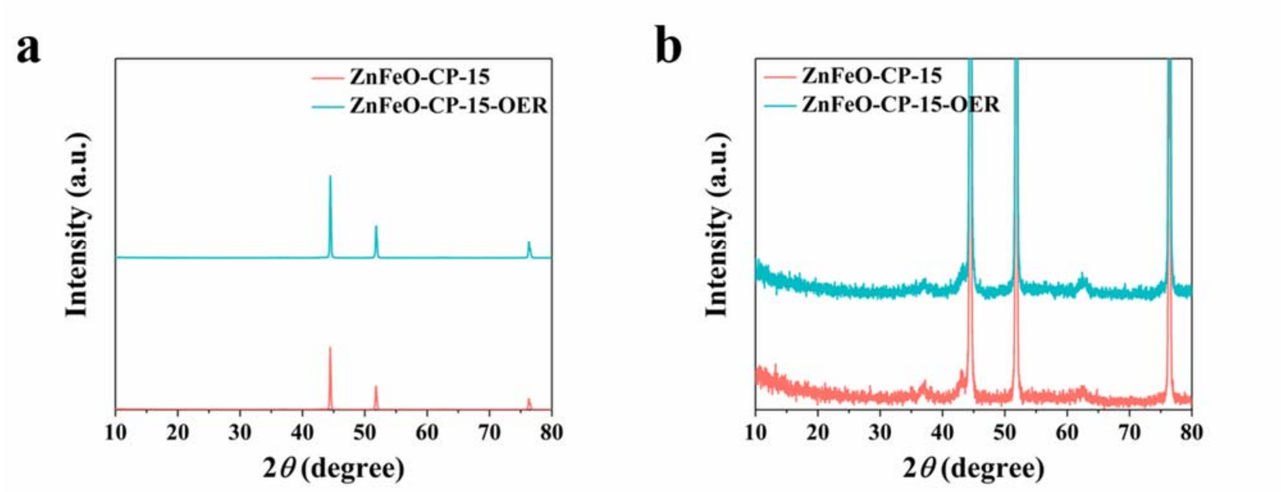

Figure S29. (a) XRD patterns of fresh ZnFeO-CP-15 and ZnFeO-CP-15 after OER. (b) Larger scale of XRD patterns.

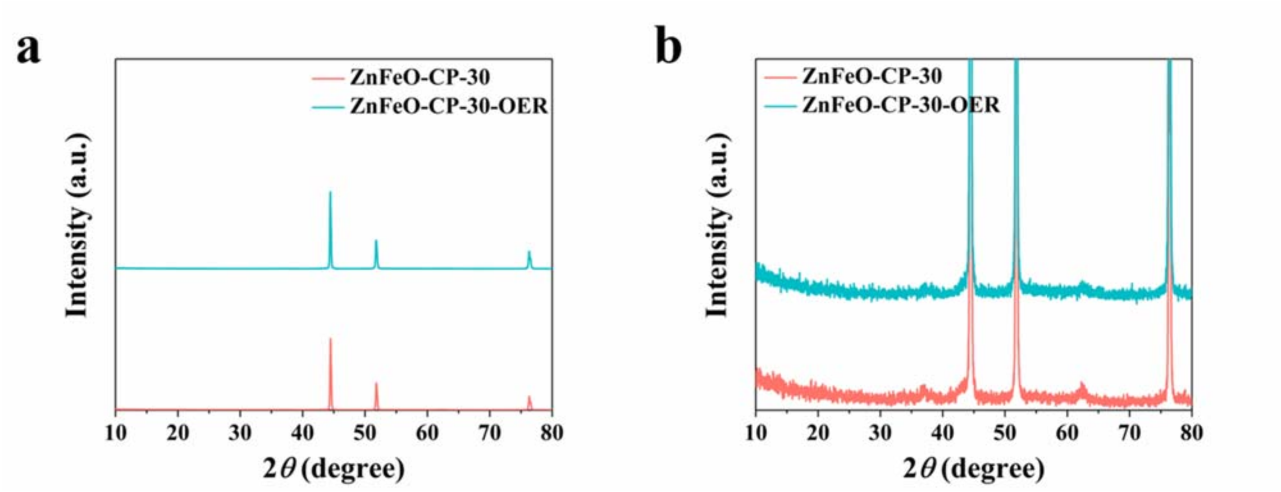

Figure S30. (a) XRD patterns of fresh ZnFeO-CP-30 and ZnFeO-CP-30 after OER. (b) Larger scale of XRD patterns.

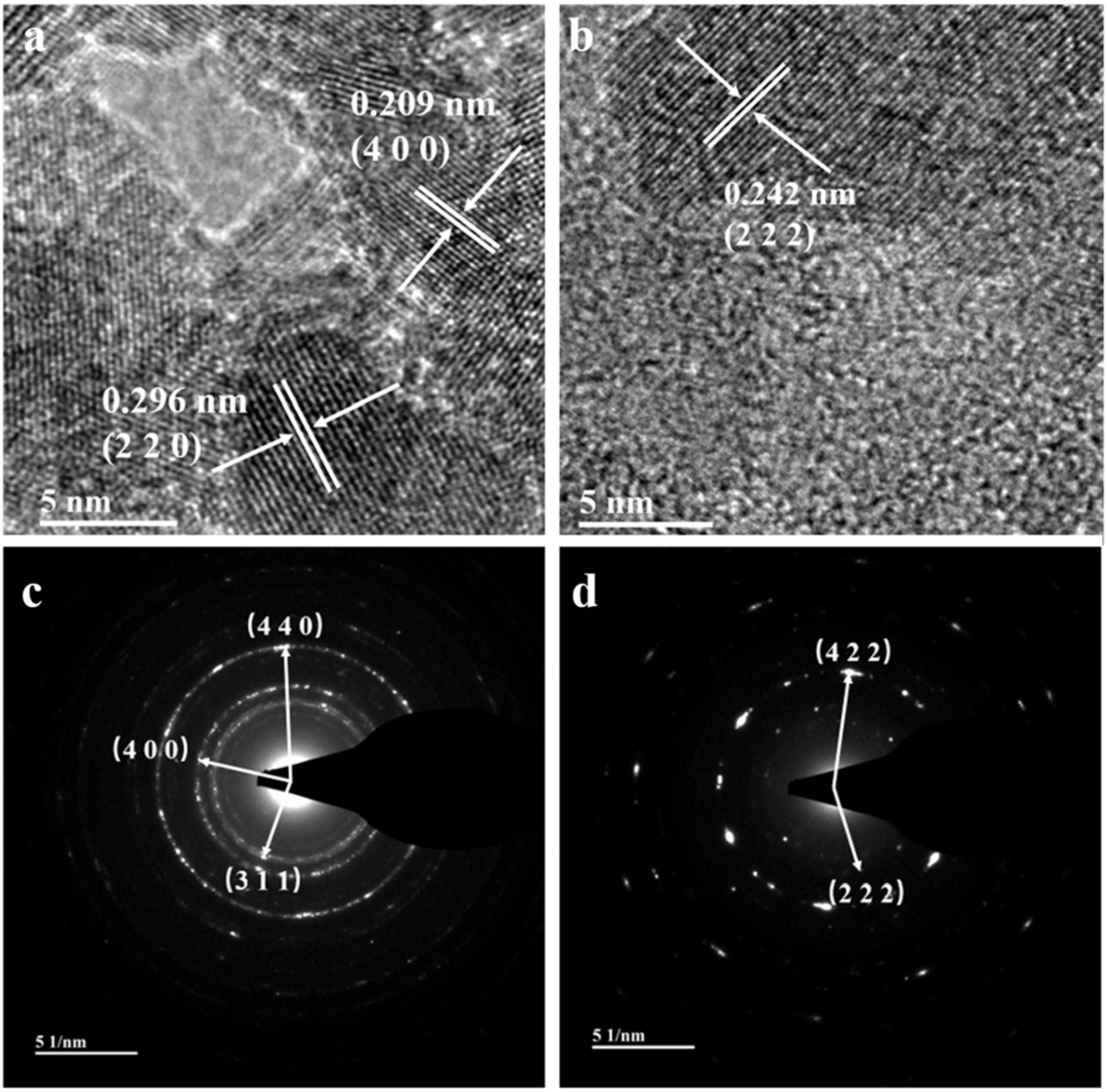

Figure S31. TEM images of (a) ZnFeO-CP-15 and (b) ZnFeO-CP-30 after OER. SAED images of (c) ZnFeO-CP-15 and (d) ZnFeO-CP-30 after OER.

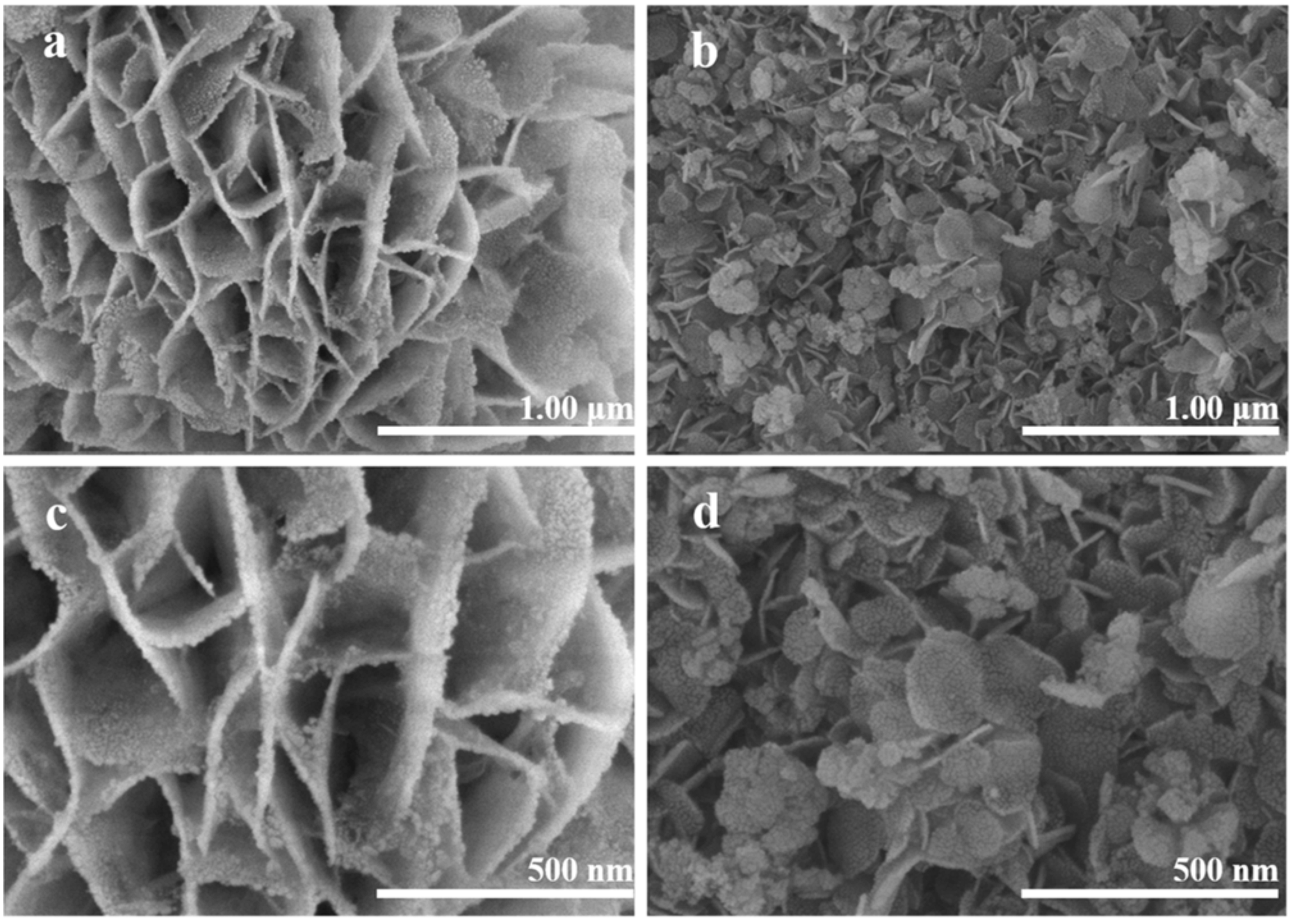

Figure S32. (a) (c) SEM image of ZnFeO-CP-15 after OER. (b) (d) SEM image of ZnFeO-CP-30 after OER.

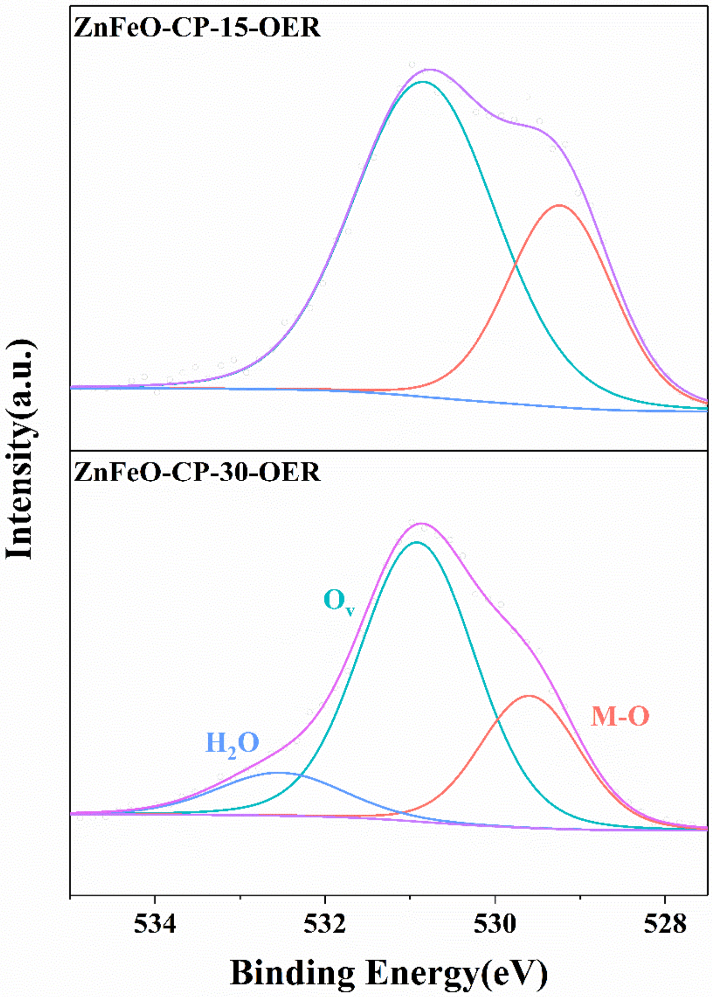

Figure S33. Deconvoluted O 1s spectra of ZnFeO-CP-15 and ZnFeO-CP-30 after OER.

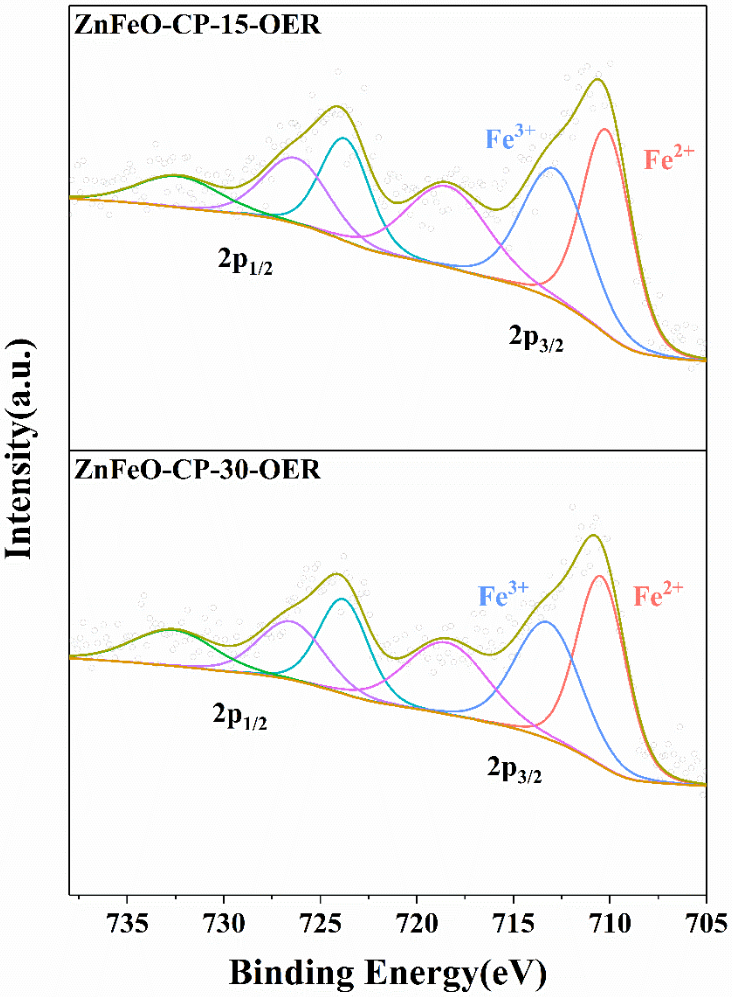

Figure S34. Deconvoluted Fe 2p spectra of ZnFeO-CP-15 and ZnFeO-CP-30 after OER.

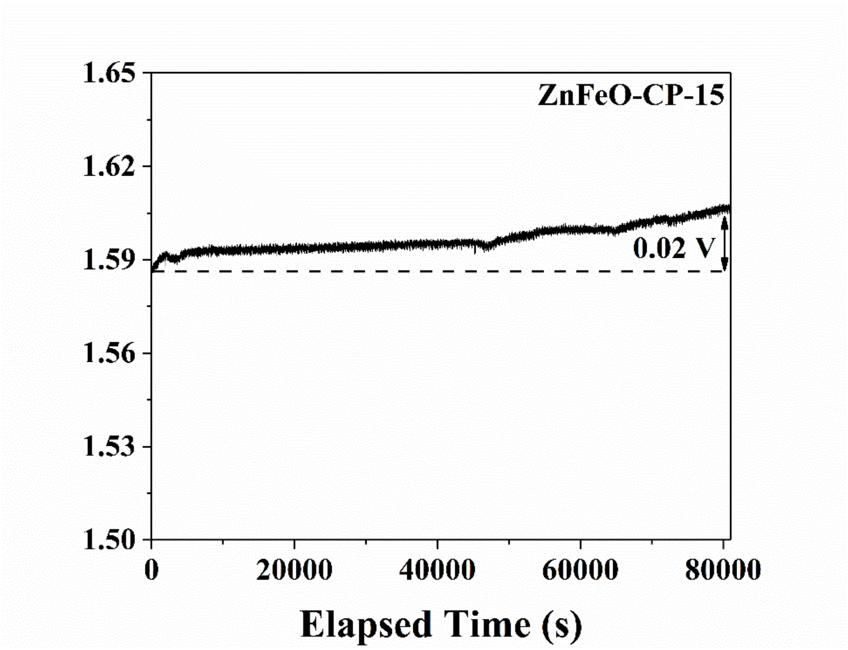

Figure S35. chronopotentiometry (CP) response curves of ZnFeO-C at a constant current of 50 mA cm^{-2}.

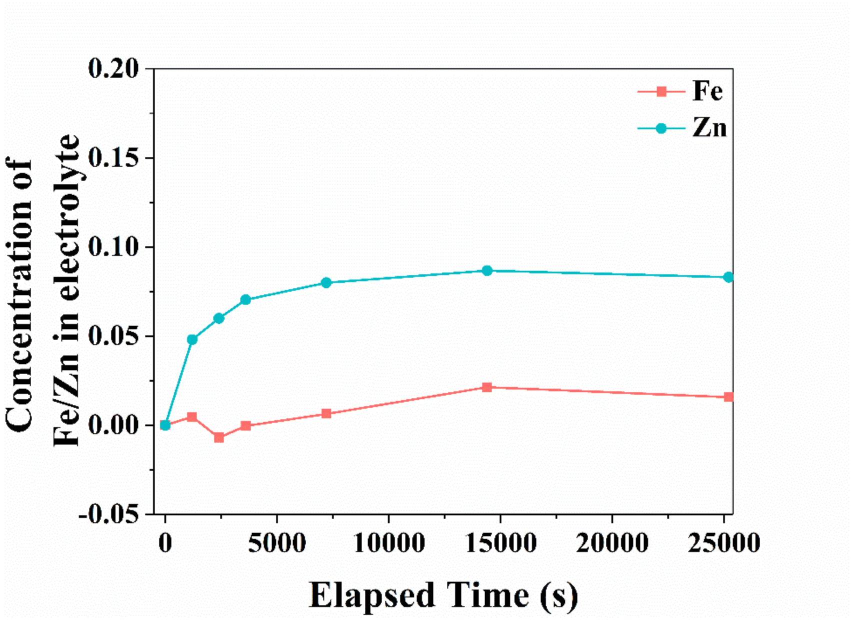

Figure S36. The Zn and Fe content in the electrolyte varies with time during the chronopotentiometry tests at 50 mA cm^{-2}. (The first point is the concentration of metal in the pure electrolyte before the reaction starts and is set to 0 mg/L for comparison purposes)

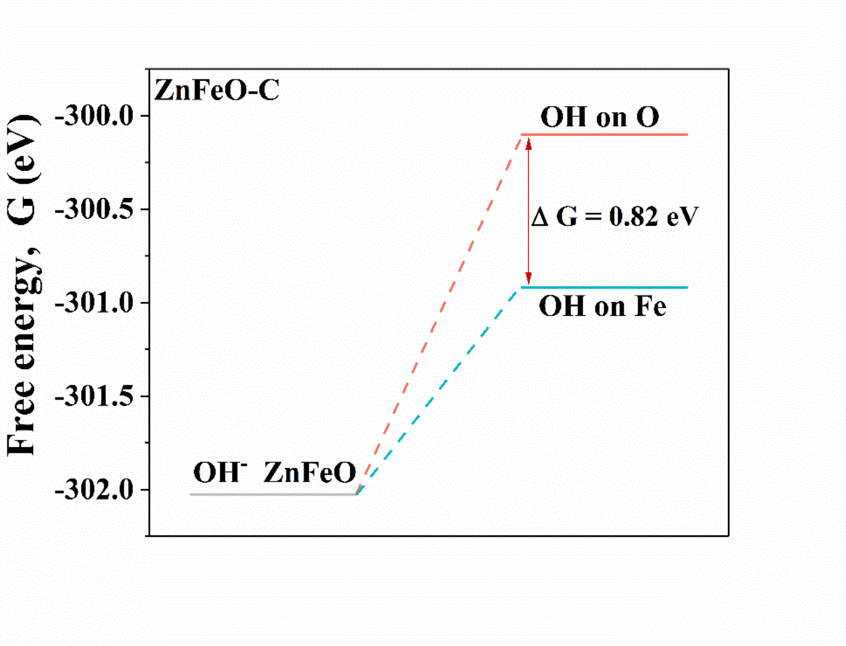

Figure S37. The free energy difference of OH$^-$ adsorbed on Fe and O for ZnFeO-C.

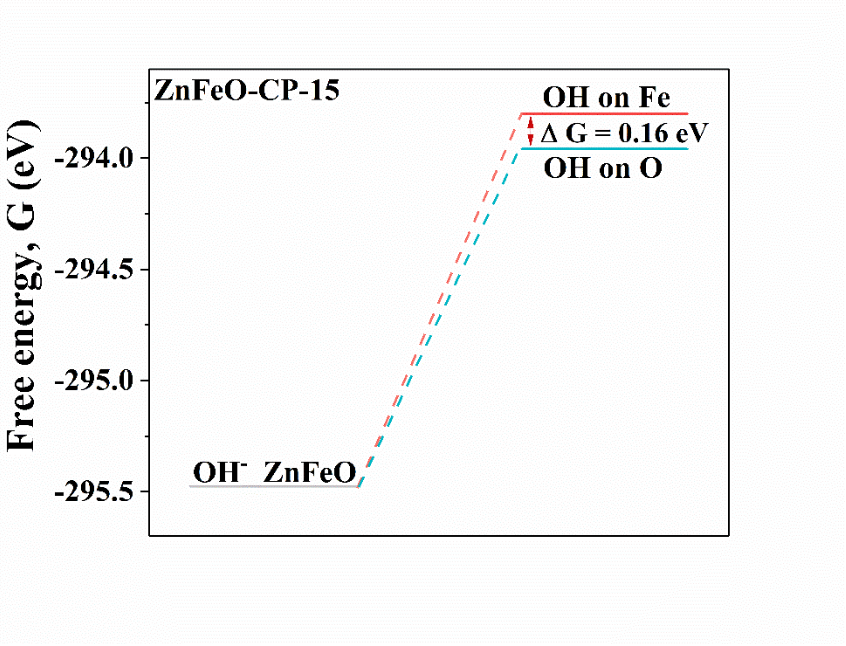

Figure S38. The free energy difference of OH$^-$ adsorbed on Fe and O for ZnFeO-CP-15

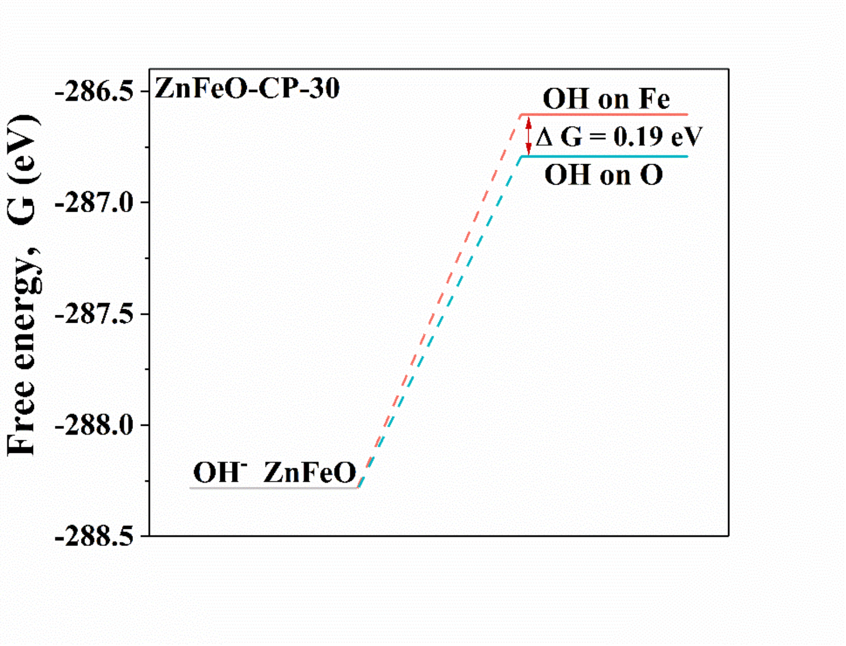

Figure S39. The free energy difference of OH^- adsorbed on Fe and O for ZnFeO-CP-30.

Table S1 Fitted Parameters of Fe K-edge EXAFS Curves of Fe foil.

Sample	Path	R(Å) [a]	$S0^2$ [b]	CN [c]	δ^2 [d]	R factor [e]
Fe foil	Fe-Fe1	2.47(0.009)	0.94(0.02)	8	0.006(0.0004)	0.30 %
	Fe-Fe_2	2.83(0.015)		6	0.007(0.0010)	

[a] Actual distance to the coordination atoms. [b] Amplitude attenuation factor. [c] Coordination number of neighboring atoms. The CN was fixed as 8 and 6 for Fe-Fe_1 and Fe-Fe_2, respectively. [d] Mean-square disorder of neighbor distance. [e] The error of fitting. Values in parentheses are uncertainties.

Table S2 Elemental compositions of ZnFeO-0.25-C and ZnFeO-0.25-CP-15 determined by XPS

Sample	Zn	Fe	O	(Zn+Fe)/O
ZnFeO-0.25-C	0.050	0.238	0.712	0.405
ZnFeO-0.25-CP-15	0.029	0.246	0.725	0.380

Table S3 The ratios of Fe^{3+}/Fe^{2+} and $O_V/O_{M\text{-}O}$ determined by XPS

Sample	Fe^{3+}/Fe^{2+}	$O_V/O_{M\text{-}O}$
ZnFeO-C	0.546	0.476
ZnFeO-CP-15	1.118	1.962
ZnFeO-CP-30	1.262	1.796
ZnFeO-0.25-C	0.398	0.486
ZnFeO-0.25-CP-15	0.483	1.976

Table S4 Elemental compositions of ZnFeO-CP-15 and ZnFeO-CP-30 after OER determined by XPS

Sample	Zn	Fe	O	(Zn+Fe)/O
ZnFeO-CP-15-OER	0.035	0.258	0.707	0.414
ZnFeO-CP-30-OER	0.029	0.156	0.815	0.227

Table S5 The ratios of Fe^{3+}/Fe^{2+} and O_V/O_{M-O} of ZnFeO-CP-15 and ZnFeO-CP-30 after OER determined by XPS

Sample	Fe^{3+}/Fe^{2+}	O_V/O_{M-O}
ZnFeO-CP-15	0.855	2.122
ZnFeO-CP-30	0.822	2.436

Table S6. Comparison of the OER activity of the ZnFeO-CP-15 with other electrocatalysts.

Catalysts	Overpotential (mV)	Tafel slope (mV dec^{-1})	Ref
ZnFeO-CP-15	236	67	Our work
P-Co_3O_4	280	52	[16]
Co/β-Mo_2C@N-CNTs	356	67	[17]
Co-300	268	38	[18]
NiCo-Air	340	75	[19]
Co_3O_4/N -rmGO	310	67	[20]
Ag@Co$(OH)_x$/CC	250	76	[21]
2D MOF-Fe/Co(1:2)	238	52	[22]
Co-Ni-Ru-S-Se (1:1:0.5:1:1)	261	52	[23]
Co@bCNTs	330	113	[24]
Co 4mmol/NC	400	100	[25]
(Ni,Co)Se_2/$CoSe_2$/NF	255	62	[26]
Co_9S_8-Ni_3S_2-CNTs/NF	127	56	[27]
NiCoP/NF	280	87	[28]
DE-TDAP	346	67	[29]
MNC-P/NF	289	85	[30]
$MnFe_2O_4$	310	65	[31]
NiFeGaOn	325	-	[32]
NiCo@NiCoO NTAs/CFC	201	39	[33]
CoFeZr	248	54	[34]
NFO/NF	309 (100 mA cm^{-2})	40	[35]
f-$Ni_{0.1}Co_{0.9}O_x$	268	70	[36]
HO_{oct}-NFO NC/IF	260	36	[37]
Co/Fe 32-red	339	41	[38]

Table S7 Calculated $\Delta E_{\mathrm{ZPE}} + \Delta U_{(0\rightarrow \mathrm{T})} - \mathrm{T}\Delta S$

Species	$\Delta E_{\mathrm{ZPE}} + \Delta U_{(0\rightarrow \mathrm{T})} - \mathrm{T}\Delta S$	
	AEM	LOM
OH* on ZnFeO-C	0.318	0.322
O* on ZnFeO-C	0.016	0.017
OOH* on ZnFeO-C	0.294	-
V_O ZnFeO-C	-	0
OH* on V_O ZnFeO-C	-	0.301
OH* on ZnFeO-CP-15	0.289	0.322
O* on ZnFeO-CP-15	0.013	0.030
OOH* on ZnFeO-CP-15	0.338	-
V_O ZnFeO-CP-15	-	0
OH* on V_O ZnFeO-CP-15	-	0.344
OH* on ZnFeO-CP-30	0.285	0.336
O* on ZnFeO-CP-30	0.015	0.050
OOH* on ZnFeO-CP-30	0.341	-
V_O ZnFeO-CP-30	-	0
OH* on V_O ZnFeO-CP-30	-	0.336

References

1. B. Ravel and M. Newville, *J. Synchrotron Radiat.*, 2005, **12**, 537-541.
2. C. Wei, S. Sun, D. Mandler, X. Wang, S. Z. Qiao and Z. J. Xu, *Chem. Soc. Rev.*, 2019, **48**, 2518-2534.
3. Kresse and Hafner, *Phys. Rev. B*, 1993, **47**, 558-561.
4. G. Kresse and J. Furthmüller, *Comput. Mater. Sci.*, 1996, **6**, 15-50.
5. J. P. Perdew, K. Burke and M. Ernzerhof, *Phys. Rev. Lett.*, 1996, **77**, 3865--3868.
6. Blochl, *Phys. Rev. B*, 1994, **50**, 17953-17979.
7. G. Kresse and D. Joubert, *Phys. Rev. B*, 1999, **59**, 1758-1775.
8. S. L. Dudarev, G. A. Botton, S. Y. Savrasov, C. J. Humphreys and A. P. Sutton, *Phys. Rev. B*, 1998, **57**, 1505-1509.
9. S. Grimme, J. Antony, S. Ehrlich and H. Krieg, *J. Chem. Phys.*, 2010, **132**, 154104.
10. S. Grimme, S. Ehrlich and L. Goerigk, *J. Comput. Chem.*, 2011, **32**, 1456-1465.
11. X. Xie, Y. Li, Z. Q. Liu, M. Haruta and W. Shen, *Nature*, 2009, **458**, 746-749.
12. J. K. Nørskov, J. Rossmeisl, A. Logadottir and L. Lindqvist, *J. Phys. Chem. B*, 2004, **108**, 17886-17892.
13. Y. Zhu, H. A. Tahini, Z. Hu, Z. G. Chen, W. Zhou, A. C. Komarek, Q. Lin, H. J. Lin, C. T. Chen, Y. Zhong, M. T. Fernandez-Diaz, S. C. Smith, H. Wang, M. Liu and Z. Shao, *Adv. Mater.*, 2020, **32**, e1905025.
14. V. Wang, N. Xu, J.-C. Liu, G. Tang and W.-T. Geng, *Comput. Phys. Commun.*, 2021, **267**, 108033.
15. J. Rossmeisl, J. K. Norskov, C. D. Taylor, M. J. Janik and M. Neurock, *J. Phys. Chem. B*, 2006,

110, 21833-21839.

16. Z. Xiao, Y. Wang, Y.-C. Huang, Z. Wei, C.-L. Dong, J. Ma, S. Shen, Y. Li and S. Wang, *Energy Environ. Sci.*, 2017, **10**, 2563-2569.

17. T. Ouyang, Y. Q. Ye, C. Y. Wu, K. Xiao and Z. Q. Liu, *Angew. Chem. Int. Ed.*, 2019, **58**, 4923-4928.

18. R. Zhang, Y.-C. Zhang, L. Pan, G.-Q. Shen, N. Mahmood, Y.-H. Ma, Y. Shi, W. Jia, L. Wang, X. Zhang, W. Xu and J.-J. Zou, *ACS Catal.*, 2018, **8**, 3803-3811.

19. W. J. Liu, J. Bao, L. Xu, M. L. Guan, Z. L. Wang, J. X. Qiu, Y. P. Huang, J. X. Xia, Y. C. Lei and H. M. Li, *Appl. Surf. Sci.*, 2019, **478**, 552-559.

20. Y. Liang, Y. Li, H. Wang, J. Zhou, J. Wang, T. Regier and H. Dai, *Nat. Mater.*, 2011, **10**, 780-786.

21. Z. Zhang, X. Li, C. Zhong, N. Zhao, Y. Deng, X. Han and W. Hu, *Angew. Chem. Int. Ed. Engl.*, 2020, **59**, 7245-7250.

22. K. Ge, S. Sun, Y. Zhao, K. Yang, S. Wang, Z. Zhang, J. Cao, Y. Yang, Y. Zhang, M. Pan and L. Zhu, *Angew. Chem. Int. Ed. Engl.*, 2021, **60**, 12097-12102.

23. W. Deng, W. Xie, D. Li, Y. Gai, Z. Chen, J. Yu, R. Yang, X. Bao and F. Jiang, *NPG Asia Mater.*, 2022, **14**, 25.

24. Z. Li, X. Lin, W. Xi, M. Shen, B. Gao, Y. Chen, Y. Zheng and B. Lin, *Appl. Surf. Sci.*, 2022, **593**, 153446.

25. S. Kim, S. Ji, H. Yang, H. Son, H. Choi, J. Kang and O. L. Li, *Appl. Catal., B*, 2022, **310**, 121361.

26. J. Zhu, Y. Lu, X. Zheng, S. Xu, S. Sun, Y. Liu, D. Li and D. Jiang, *Appl. Surf. Sci.*, 2022, **592**, 153352.

27. Y. Yao, J. He, L. Ma, J. Wang, L. Peng, X. Zhu, K. Li and M. Qu, *J. Colloid Interface Sci.*, 2022, **616**, 287-297.

28. H. Liang, A. N. Gandi, D. H. Anjum, X. Wang, U. Schwingenschlogl and H. N. Alshareef, *Nano Lett.*, 2016, **16**, 7718-7725.

29. G. Yasin, S. Ibraheem, S. Ali, M. Arif, S. Ibrahim, R. Iqbal, A. Kumar, M. Tabish, M. A. Mushtaq, A. Saad, H. Xu and W. Zhao, *Mater. Today Chem.*, 2022, **23**, 100634.

30. K. E. Salem, A. A. Saleh, G. E. Khedr, B. S. Shaheen and N. K. Allam, *Energy Environ. Mater.*, 2022, 12324.

31. J. Kim, J. Lee, C. Liu, S. Pandey, S. Woo Joo, N. Son and M. Kang, *Appl. Surf. Sci.*, 2021, **546**, 149124.

32. F. A. Garces-Pineda, H. Chuong Nguyen, M. Blasco-Ahicart, M. Garcia-Tecedor, M. de Fez Febre, P. Y. Tang, J. Arbiol, S. Gimenez, J. R. Galan-Mascaros and N. Lopez, *ChemSusChem*, 2021, **14**, 1595-1601.

33. Y. Liu, Y. Ying, L. Fei, Y. Liu, Q. Hu, G. Zhang, S. Y. Pang, W. Lu, C. L. Mak, X. Luo, L. Zhou, M. Wei and H. Huang, *J. Am. Chem. Soc.*, 2019, **141**, 8136-8145.

34. L. Huang, D. Chen, G. Luo, Y. R. Lu, C. Chen, Y. Zou, C. L. Dong, Y. Li and S. Wang, *Adv. Mater.*, 2019, **31**, e1901439.

35. L. Gao, X. Cui, Z. Wang, C. D. Sewell, Z. Li, S. Liang, M. Zhang, J. Li, Y. Hu and Z. Lin, *Proc. Natl. Acad. Sci. U. S. A.*, 2021, **118**, e2023421118.

36. X. Yu, C. Hu, P. Ji, Y. Ren, H. Zhao, G. Liu, R. Xu, X. Zhu, Z. Li, Y. Ma and L. Ma, *Appl. Catal., B*, 2022, **310**, 121301.

37. Y. Peng, C. Huang, J. Huang, M. Feng, X. Qiu, X. Yue and S. Huang, *Adv. Funct. Mater.*, 2022, 2201011.

38. E. Budiyanto, S. Salamon, Y. Wang, H. Wende and H. Tueysuez, *Jacs Au*, 2022, **2**, 697-710.